

RESEARCH ARTICLE

10.1002/2014WR016427

Key Points:

- A long-term evolution in rock permeability is measured
- The increase in permeability in the intact samples is likely due to the formation of flow paths
- The decrease in permeability in the fractured samples is attributed to the dissolution at the contacting asperities

Correspondence to:

H. Yasuhara,
hide@cee.ehime-u.ac.jp

Citation:

Yasuhara, H., N. Kinoshita, H. Ohfuji, M. Takahashi, K. Ito, and K. Kishida (2015), Long-term observation of permeability in sedimentary rocks under high-temperature and stress conditions and its interpretation mediated by microstructural investigations, *Water Resour. Res.*, 51, 5425–5449, doi:10.1002/2014WR016427.

Received 23 SEP 2014

Accepted 14 JUN 2015

Accepted article online 17 JUN 2015

Published online 14 JUL 2015

Long-term observation of permeability in sedimentary rocks under high-temperature and stress conditions and its interpretation mediated by microstructural investigations

Hideaki Yasuhara¹, Naoki Kinoshita¹, Hiroaki Ohfuji², Manabu Takahashi³, Kazumasa Ito³, and Kiyoshi Kishida⁴

¹Department of Civil and Environmental Engineering, Ehime University, Matsuyama, Japan, ²Geodynamics Research Center, Ehime University, Matsuyama, Japan, ³National Institute of Advanced Industrial Science and Technology, Tsukuba, Japan, ⁴Department of Urban Management, Kyoto University, Kyoto, Japan

Abstract In this study, a series of long-term, intermittent permeability experiments utilizing Berea sandstone and Horonobe mudstone samples, with and without a single artificial fracture, is conducted for more than 1000 days to examine the evolution of rock permeability under relatively high-temperature and confining pressure conditions. Effluent element concentrations are also measured throughout the experiments. Before and after flow-through experiments, rock samples are prepared for X-ray diffraction, X-ray fluorescence, and scanning electron microscopy coupled with energy dispersive X-ray spectroscopy to examine the mineralogical changes between pre and postexperimental samples, and also for microfocus X-ray CT to evaluate the alteration of the microstructure. Although there are exceptions, the observed, qualitative evolution of permeability is found to be generally consistent in both the intact and the fractured rock samples—the permeability in the intact rock samples increases with time after experiencing no significant changes in permeability for the first several hundred days, while that in the fractured rock samples decreases with time. An evaluation of the Damkohler number and of the net dissolution, using the measured element concentrations, reveals that the increase in permeability can most likely be attributed to the relative dominance of the mineral dissolution in the pore spaces, while the decrease can most likely be attributed to the mineral dissolution/crushing at the propping asperities within the fracture. Taking supplemental observations by microfocus X-ray CT and using the intact sandstone samples, a slight increase in relatively large pore spaces is seen. This supports the increase in permeability observed in the flow-through experiments.

1. Introduction

An understanding of the flow and transport characteristics of porous/fractured rocks is required for the safe and long-term geological isolation of energy-related by-products (i.e., high-level radioactive waste and anthropogenic CO₂). Notably, under elevated temperature and stress conditions, mechanically and chemically mediated processes may alter the pore structure in rocks, resulting in an irreversible evolution of the flow and transport behavior. An augmentation in permeability may result from the mechanical dilation brought about by shearing and/or mineral dissolution within the pore spaces, while a reduction in it may result from reversible or irreversible mechanical compaction, mineral dissolution at the contacting areas, and/or the clogging of pore spaces by the precipitation of secondary minerals.

A chemo-mechanically coupled compaction process can result in a reduction in permeability and may include the growth of subcritical cracks. This means that cracks propagate with time even when the exerted stress at the contacts is smaller than the fracture toughness [e.g., Lawn and Wilshaw, 1975; Atkinson, 1984; Atkinson and Meredith, 1987; Scholz, 1990; Lockner, 1993; Yasuhara and Elsworth, 2008; Røyne et al., 2011; Brantut et al., 2013]. The process may also include a pressure solution, which incorporates three serial processes—mineral dissolution at the stressed contacts, diffusive transport through the thin film of water, and reprecipitation of the mineral matter at the pore wall [e.g., Weyl, 1959; Rutter, 1976; Robin, 1978; Raj, 1982; Dewers and Hajash, 1995; Spiers et al., 2003; Zubtsov et al., 2004; Croizé et al., 2010, 2013; Zhang et al., 2010, 2011; Neveux et al., 2014a, 2014b]. The pressure solution affects the changes in permeability even under

moderate stress (<10 MPa) and temperature (<150°C) conditions [Polak *et al.*, 2003, 2004; Yasuhara *et al.*, 2004, 2006, 2011].

In contrast, a pure chemically mediated process of the free-face dissolution can sometimes bring about the formation of wormholes and may cause an increase in permeability with time. It has been investigated in porous media [e.g., Hung *et al.*, 1989; Fredd and Fogler, 1999; Panga *et al.*, 2005; Kalia and Balakotaiah, 2009] and in fractured media [e.g., Durham *et al.*, 2001; Polak *et al.*, 2004; Szymczak and Ladd, 2009; Ishibashi *et al.*, 2013; Elkhoury *et al.*, 2013]. These studies were typically performed in carbonate porous/fractured media. Experimental studies performed in rock other than carbonate rock are relatively sparse, although there are some examples of studies conducted in granite [Moore *et al.*, 1994], novaculite [Polak *et al.*, 2003; Yasuhara *et al.*, 2006], and sandstone [Walsh *et al.*, 2014].

In all the above mentioned works, the changes in permeability have been observed over relatively short periods, namely, from a few hours to several months. When considering the long-term integrity of the rocks of interest in the geological isolation of high-level radioactive waste and anthropogenic CO₂, the longer evolution of the permeability should be examined in detail, and the mechanism explaining the longer changes in permeability should be understood. To this end, we have observed the changes in permeability for far longer periods (i.e., >1000 days) in two kinds of sedimentary rocks, namely, Berea sandstone and Horonobe mudstone. Sandstone formations are potential reservoirs of CO₂ geo-sequestration, and Berea sandstone is popular in research works related to engineering geology. Thus, a lot of data (e.g., physical properties) are available in the literature. On the other hand, mudstone formations are potential sites for high-level radioactive waste. Horonobe mudstone can be obtained from the Horonobe Underground Research Laboratory site in Japan where the Horonobe Underground Research Center has conducted research and development on the geological disposal of high-level radioactive waste. This is the reason we have chosen these two types of sedimentary rocks for the present study.

In this work, a series of permeability experiments on intact core samples of Berea sandstone and on single-fracture core samples of both Berea sandstone and Horonobe mudstone has been conducted under different confining pressure and temperature conditions. The experiments follow the progress of the permeability utilizing the intermittent measurements of the evolving flow rate and the effluent mineral mass. In the case of the sandstone experiments, deionized water is used as the permeant fluid, which can dissolve a greater amount of minerals than groundwater because of its low activity. Deionized water is used instead of groundwater because it enables the straightforward analysis of the effluent element concentrations in effluent solutions and because the evolution of permeability mediated by the mineral dissolution may be more readily observable. In the case of the mudstone experiments, two different permeants are employed, namely, deionized water and silicon oil. Silicon oil is used to inhibit subcritical crack growth and pressure solution, and such a configuration may enable examination and understanding of mechanical creep, which can be observed as a reduction in permeability, occurs under stressed conditions. Petrographic and microstructural observations are also conducted by adopting X-ray diffraction (XRD), X-ray fluorescence (XRF), SEM-EDX, and microfocus X-ray CT to examine the mechanisms that explain the changes in permeability measured from the permeability experiments.

2. Experimental Method

A series of permeability experiments was conducted on cylindrical intact samples of Berea sandstone (30 mm in diameter × 60 mm in length) and on samples of Berea sandstone and Horonobe mudstone containing a single diametric saw-cut fracture along the cylindrical axis, as shown in Figure 1. Note that all the cores of both the Berea sandstone and the Horonobe mudstone were cored perpendicular to the bedding planes, meaning that the flow direction in the permeability experiments was also perpendicular to them. Two kinds of permeants (i.e., deionized water and silicon oil) were adopted in this work. The oil flow experiment was conducted to examine the effect of mechanical creep on the changes in permeability under no mineral-dissolution conditions. The mechanical creep may be enhanced under wet conditions [Lockner, 1995; Masuda, 2001], but it should be due to chemical effects. Therefore, the oil flow experiment enables the extraction of the mechanical effects on the changes in permeability. Throughout each permeability experiment, the measured flow rate yielded an intermittent record of averaged rock transmissivity, which was converted to the average permeability. Preexperimental analyses were conducted on the rock samples to obtain the mineralogical and chemical compositions by XRD and XRF, respectively. The *P* wave velocity,

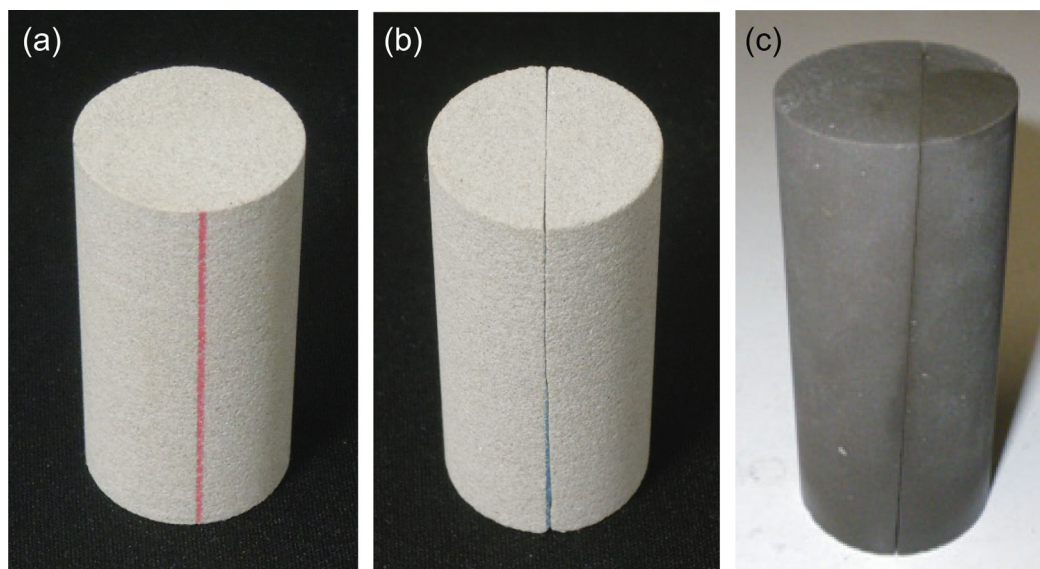


Figure 1. Rock samples. (a) Intact Berea sandstone, (b) Berea sandstone with a fracture, and (c) Horonobe mudstone with a fracture; 30 mm in diameter × 60 mm in length.

which is directly related to the elastic properties of the materials whose higher *P* wave velocity represents a stiffer body, was also measured for the sandstone samples before the commencement of the permeability experiments. Moreover, the pore size distribution and the microstructure of the sandstone samples were obtained by microfocus X-ray CT supplemented with mercury porosimetry.

2.1. Rock Samples

The representative chemical compositions of the sandstone and mudstone samples were determined by XRF. The weight percentages of the major elements are listed in Table 1. In addition, the mineral compositions of the sandstone and the mudstone samples, before the permeability experiments, were also determined by XRD and are shown in Figure 2. Berea sandstone is composed almost completely of pure quartz, but also contains slight amounts of feldspars, dolomite, and kaolinite. Meanwhile, Horonobe mudstone, recovered from the Wakkanai Formation at the Horonobe Underground Research Laboratory (URL), Japan, is mineralogically more complex; it is composed mainly of quartz, opal-A, and opal-CT, and partly of feldspars, calcite, illite, and chlorite. In this study, the clay fraction of the mudstone was not identified, but was thought to be much smaller than the amount of nonclay minerals [Hama *et al.*, 2007; Kurikami *et al.*, 2008]. Notably, the rock samples contain a relatively large amount of opal minerals; this finding is consistent with the results reported by Tachi *et al.* [2011].

The surfaces of the saw cut fractures of Berea sandstone and Horonobe mudstone were measured through laser profiling (KEYENCE KS-1100) with a vertical resolution of 0.1 μm on a rectangular lateral grid of 20 μm,

Oxide	Berea Sandstone Results (wt %)	Horonobe Mudstone Results (wt %)
SiO ₂	82.6	71.2
Al ₂ O ₃	9.88	10.7
Fe ₂ O ₃	2.13	6.78
SO ₃		3.26
K ₂ O	1.97	2.78
CaO	1.66	1.00
MgO	0.973	1.51
Na ₂ O		1.51
TiO ₂	0.633	0.876
Cl		0.239
Others	0.154	0.241

as shown in Figure 3. The measured distributions of surface elevation are Gaussian, and the standard deviations of Berea sandstone and Horonobe mudstone are 59.7 and 36.7 μm, respectively. All the fractures were saw cut using the same procedure, but the surfaces of the Berea sandstone are rougher than those of the Horonobe mudstone, which is attributed to the size of the grains composing the rocks.

2.2. Experimental Setup

The setup for the permeability experiments is shown in Figure 4. Before setting the rock samples within a pressure cell, the samples for the

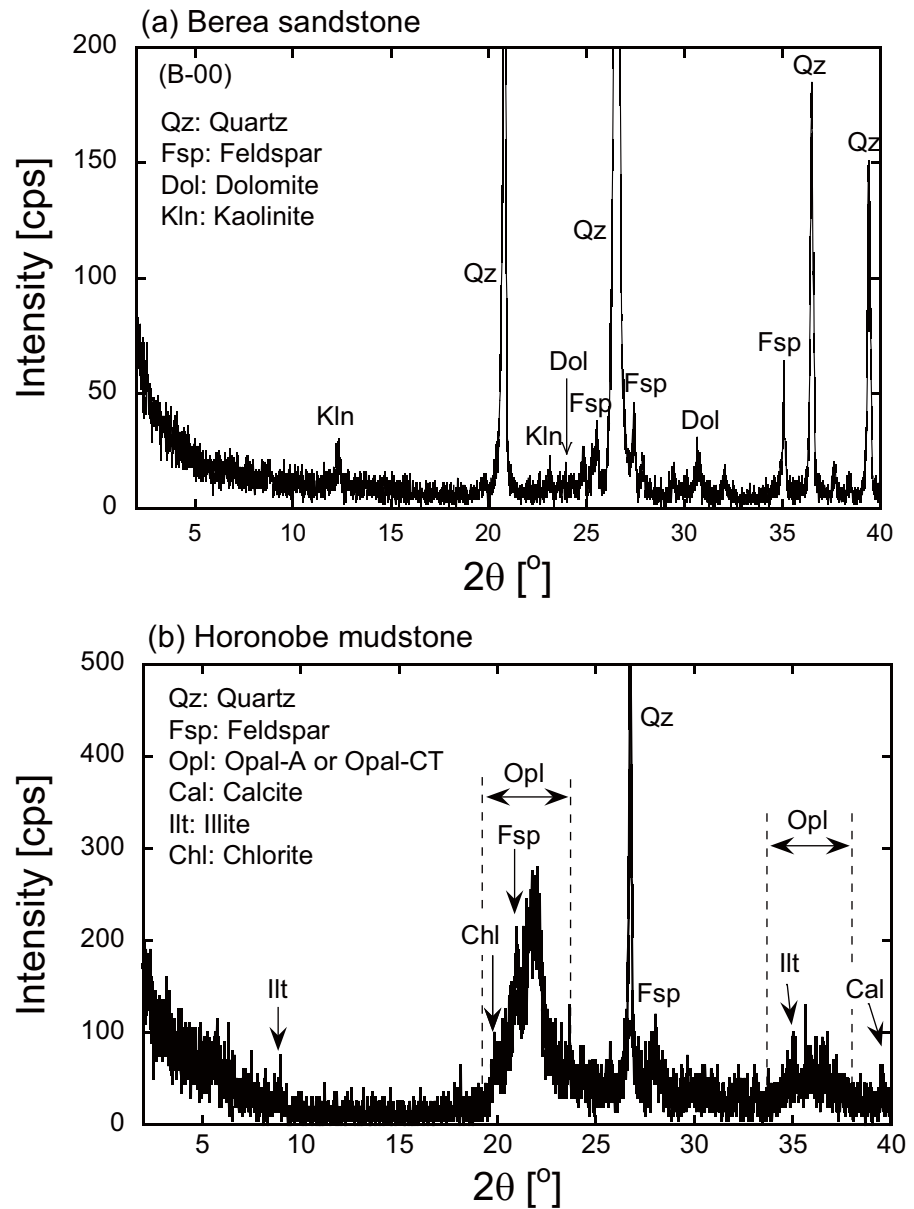


Figure 2. Mineral composition of rock samples determined by XRD. (a) Berea sandstone and (b) Horonobe mudstone.

water flow experiments were immersed in a beaker filled with deionized water and then placed inside a desiccator. Subsequently, the space in the desiccator was evacuated by a vacuum pump for 6 h in order to remove air from the rock samples. On the other hand, the samples for the oil flow experiments were immersed in silicon oil and then left at atmospheric pressure for 2–3 days. It should be noted that the air within sample H-5 was not evacuated by a vacuum pump because the pump is susceptible to malfunctions due to the vaporized oil. Therefore, the samples immersed in silicon oil were not saturated. After the saturation process, the two half-rock samples were carefully fitted together to avoid introducing any small debris into the fracture. Then, the fitted core was confined within a heat-shrink tube. Once the core was jacketed, it was placed inside a pressure cell. Subsequently, axial pressure was prescribed by disc springs and controlled well by a load cell mounted onto the springs (Figure 4). Confining pressure, equivalent to the axial pressure, was applied by a hand pump and controlled by a regulator. Data on the evolving axial and confining pressures were recorded at 5 s intervals and monitored with data loggers and digital indicators to precisely maintain the prescribed pressures.

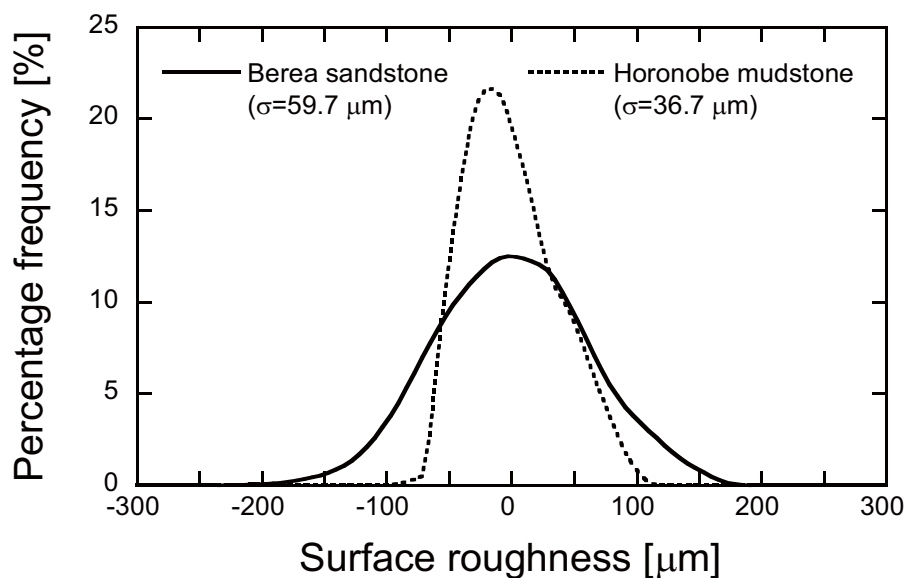


Figure 3. Distribution of surface roughness of Berea sandstone and Horonobe mudstone. A value of zero represents the mean height of the surface roughness, and σ is the standard deviation.

In the series of experiments, two different temperature conditions were set, namely, 20 and 90°C. In the case of 20°C, the pressure cells with the pressurized samples were placed in a thermostatic laboratory maintained at $20 \pm 1.0^\circ\text{C}$. In the case of 90°C, heating was conducted by submerging the pressure cells within a cylindrical container filled with heated silicon oil whose temperature was maintained at $90 \pm 0.5^\circ\text{C}$ (Figure 4). The injected fluid (i.e., deionized water or silicon oil) was preheated to 90°C by cable heaters before being injected into the core interior. A combination of preheating and efficient insulation enabled the maintenance of the temperatures of the injected fluids to be congruent to those of the pressure cells. Note that the temperatures of the rock samples were not measured, but were regarded as being the same as those of the heated silicon oil and the pressure cells.

The permeability experiments were intermittently conducted every 5 or 10 days. Note that a syringe pump was carefully connected to and disconnected from the flow tubes of the pressure cells to avoid introducing air bubbles into the cells. The flow tubes were completely plugged with end plugs, except when conducting the permeability experiments. Therefore, between the permeability experiments, no-flow conditions were maintained. On the other hand, during the permeability experiments, the pressure differential between the sample inlet and the sample outlet was controlled by the syringe pump. The flow rates were evaluated by directly weighing the effluent fluid flowing out of the pressure cells. The effluent water was collected during each permeability experiment to determine the effluent Si, Al, K, Fe, Ca, Na, Mg, Cl, and S concentrations. The amount of effluent water collected every time was 8 and 3 mL for the samples of Berea sandstone and Horonobe mudstone, respectively. Once the fixed amount was collected, each permeability experiment was halted. The initial pore volume of the sandstone evaluated from the initial porosity (i.e., $\sim 17\%$) was ~ 7 mL, and approximately one pore volume of the water was collected for the sandstone samples. Meanwhile, the amount collected for the mudstone samples (i.e., 3 mL) may be greater than that of the pore water within a fracture, and the element concentrations may be diluted to some degree. In any case, pore water was flushed each time for every permeability experiment and freshwater was injected into the samples.

2.3. Experimental Procedure

In this study, experiments using seven sandstone samples were conducted under confining pressures of 7.5 and 15 MPa, at temperatures of 20 and 90°C, and under differential water pressures of 350 kPa for the intact samples and 9.80 kPa for the fractured samples. It should be noted that the differential water pressures were evaluated by subtracting the influence of the hydrostatic pressure arising between the sample inlet and the sample outlet. The maximum hydraulic gradient induced in this system is moderately high (i.e., in the order of a few hundred), which is incongruent with the natural system of groundwater movement. Such high hydraulic gradients were reluctantly adopted in order to control the flow-through system and to obtain

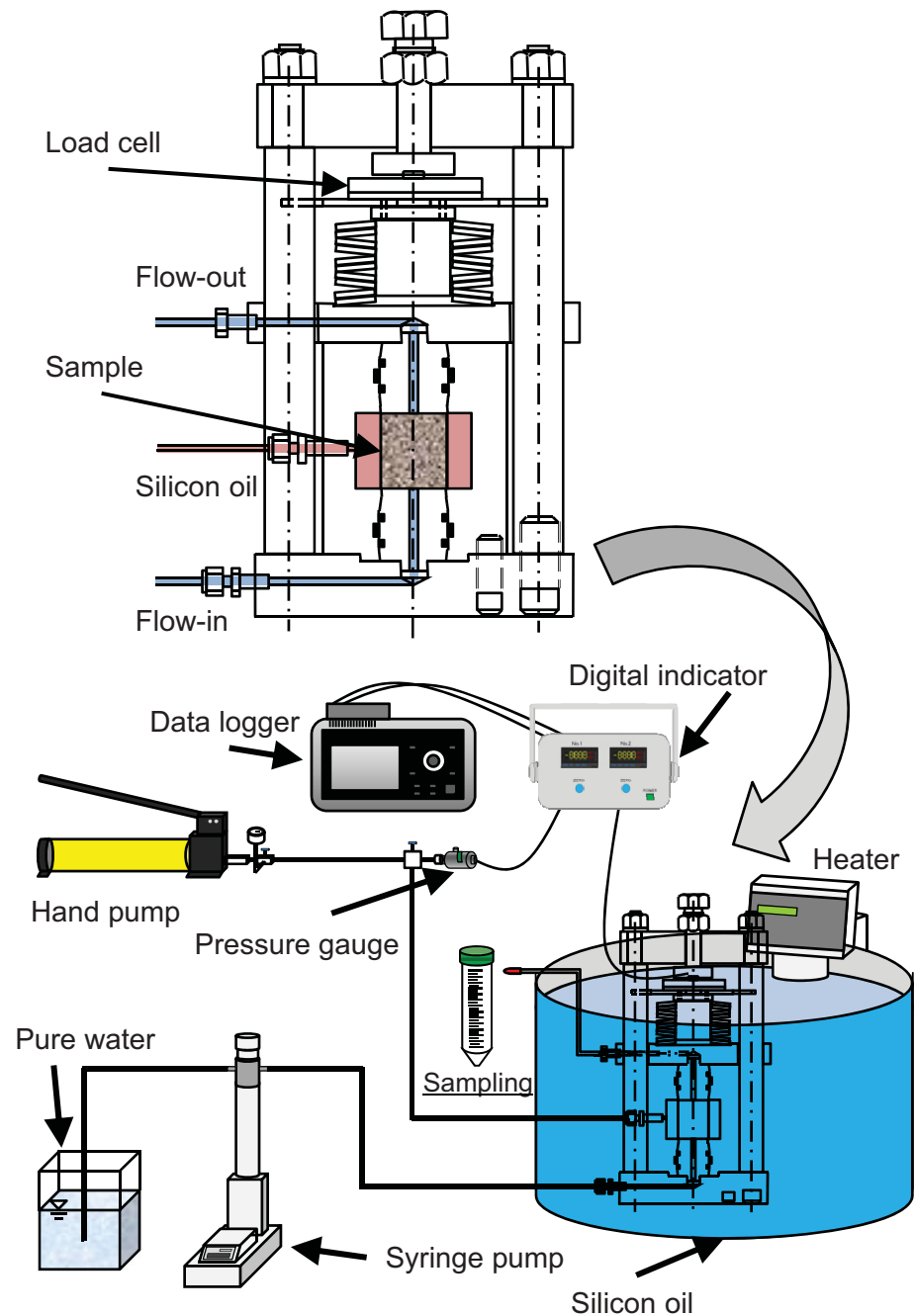


Figure 4. Schematic of experimental setup for permeability experiments.

measurable flow rates. The only permeant used in the experiments on the sandstone samples was deionized water. The permeability of the intact samples was evaluated by assuming a Darcian flow, given by

$$k = \frac{\mu QL}{A \Delta P}, \quad (1)$$

where k is the intrinsic permeability (m^2), μ is the dynamic viscosity ($Pa \cdot s$), Q is the flow rate ($m^3 \cdot s^{-1}$), L is the sample height (m), A is the cross-sectional area (m^2), and ΔP is the differential pressure (Pa). Similarly, the fracture permeability was evaluated via the hydraulic aperture obtained using a parallel plate approximation [Gangi, 1978; Witherspoon et al., 1980], namely,

Table 2. Experimental Conditions

Sample	Rock Type	Intact or Fracture	Temperature (°C)	Confining Pressure (MPa)	Differential Pressure (kPa)	Permeant	Experimental Duration (day)
B-42	Sandstone	Intact	20	7.5	350	Deionized water	1015 ^a
B-43		Intact	20	15	350	Deionized water	1080
B-44		Intact	90	15	350	Deionized water	1040
B-45		Intact	90	7.5	350	Deionized water	566 ^a
B-46		Intact	90	7.5	350	Deionized water	1020
B-47		Fracture	20	7.5	9.80	Deionized water	790
B-48		Fracture	90	7.5	9.80	Deionized water	820
H-1		Mudstone	Fracture	90	3.0	350	Deionized water
H-3	Fracture		20	3.0	350	Deionized water	470
H-5	Fracture		90	3.0	350	Silicon oil	130

^aThe experiments for B-42 and B-45 were terminated for microstructural observations, but the others are still ongoing.

$$\langle b \rangle = \left(\frac{12\mu L \cdot Q}{W \cdot \Delta P} \right)^{1/3}, \tag{2}$$

$$k = \frac{\langle b \rangle^2}{12}, \tag{3}$$

where $\langle b \rangle$ is the hydraulic aperture (m) and W is the sample width (m).

For the mudstone, three experiments were conducted under a confining pressure of 3.0 MPa, at temperatures of 25 and 90°C, and under a differential water pressure of 350 kPa. As noted in the previous section, for the mudstone experiments, two different permeants were adopted, namely, deionized water and silicon oil, that can inhibit mineral dissolution. The experimental conditions for each case are tabulated in Table 2. Through the various experiments conducted in this study, it was possible to examine the evolution of permeability in both the intact and the fractured samples with different rock types, confining pressures, temperatures, and permeants. It should also be noted that the permeability was examined for significantly long periods—the measurements were conducted for more than several 100 days in all cases and for more than 1000 days in many cases.

2.4. Chemical Analyses of Effluent Fluids

Deionized water (pH ~7) was utilized as the permeant in the permeability experiments for both the sandstone and the mudstone samples. Thus, the measured effluent element concentrations should originate from the rock samples only. As explained in the previous section, fluid samples were taken from the flow outlet at regular intervals (one sample per 5 or 10 days) to determine the effluent Si, Al, K, Fe, Ca, Na, and Mg concentrations by inductively coupled plasma atomic emission spectrometry (ICP-AES) (Thermo Scientific iCAP 6300) and the Cl⁻ and SO₄²⁻ concentrations by ion chromatography (IC) (Thermo Scientific DX-32). Prior to the ICP and IC analyses, 3 mL of the effluent solutions were diluted to 15 mL by a 2 wt % concentration of HNO₃ and by deionized water, respectively. This dilution procedure was adopted to avoid the precipitation of secondary minerals that may occur while lowering the temperature from 90°C to room temperature.

2.5. Petrographic Observations

The mineralogical alteration in the samples after the long-term permeability experiments was analyzed using a field-emission SEM (JEOL JSM-7000F), equipped with an EDX system (Oxford Instruments, X-Max 20). The SEM-EDX analysis was conducted for samples B-00, B-42, and B-45. Sample B-00 represents a preexperimental sample, and samples B-42 and B-45 underwent a confining pressure of 7.5 MPa and temperatures of 20 and 90°C for 1015 and 566 days, respectively. Prior to the SEM-EDX analysis, the core samples were completely dried at room temperature and then sliced to a thickness of ~5 mm. The shaped samples were placed on a stub and coated with a thin (10 nm) osmium layer. At particular locations where precipitated minerals were observed, an EDX analysis was conducted to identify the chemical compositions. SEM was operated at an accelerating voltage of 15 kV, and a beam current of 1 nA was used for the semiquantitative chemical analysis.

2.6. Observations of Micropores

In order to evaluate the evolution of the pore size distribution between pre and postexperiments, a microfocus X-ray CT (TESCO TXS225-ACTIS), complimented with mercury porosimetry (Micromeritics Auto pore IV9520),

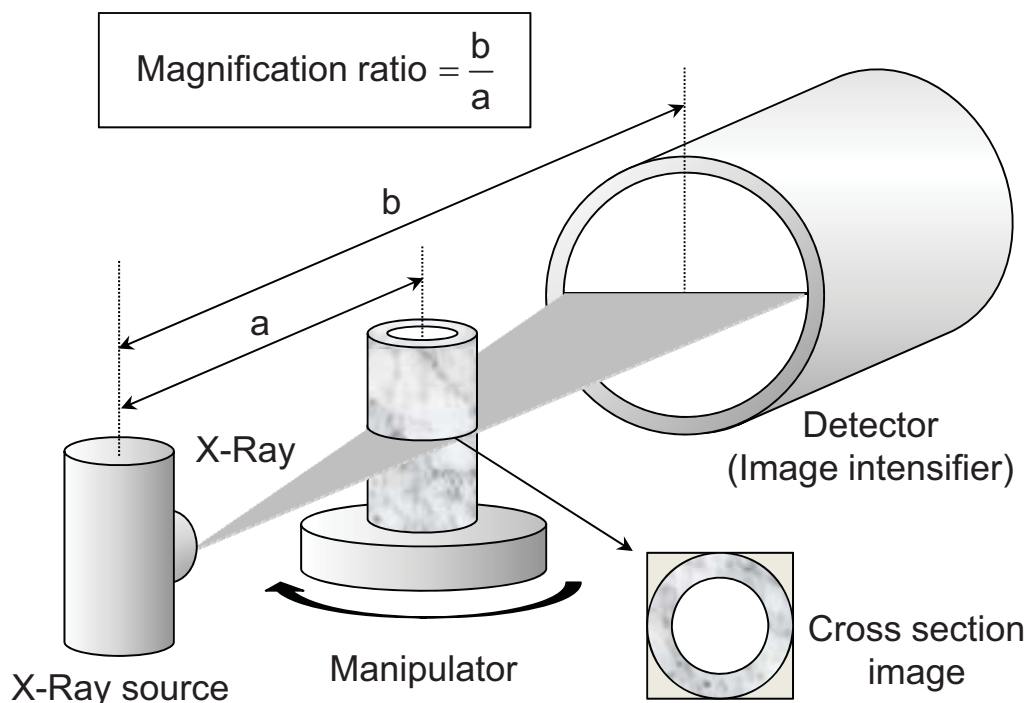


Figure 5. Schematic of microfocus X-ray CT configuration.

was performed for samples B-00, B-42, and B-45, which were also used for the SEM-EDX analysis. The internal structure of an object is determined according to the absorption rates of the X-rays transmitted to the rotating object, as schematically shown in Figure 5. The system is capable of reconstructing the two-dimensional information on any cross section. Microfocus X-ray CT is different from typical X-ray CT in that the electron beams are narrowly emitted from the X-ray radiation source. A spatial resolution of $5 \mu\text{m}$ is attained by this additional function. After taking scanned images, a threshold value should be fixed to distinguish the pore spaces and the solid particles in the rock samples. In this study, the threshold values were determined by fitting the bulk porosity, measured by mercury porosimetry, with that evaluated by the three-dimensional CT data. The spatial resolution of $5 \mu\text{m}$, attained in the CT analyses, may not be high enough to identify the shapes of all the pores that are detected by mercury porosimetry. However, the fitting procedure only enables the evaluation of the changes in pore size distribution between the pre and postexperimental samples. It should be noted that just using mercury porosimetry is not sufficient for identifying such changes, because mercury porosimetry cannot be applied to the preexperimental samples, and it ruins the internal structures of the samples if applied.

Lindquist and Venkatarangan [1999] developed a 3DMA computational package for analyzing the geometry of the pore and grain phases in three-dimensional CT data. Using this package, the spatial distributions of pore and throat sizes, the coordination number, the tortuosity, and other geometric relations can be obtained. In the 3DMA package, the kriging-based algorithm is used to segment the voxel images. The medial axis for a sphere is a straight-line passing through the center point and that for a cylinder is the axis of rotational symmetry. The medial axis for any n -dimensional object can be found by employing an algorithm equivalent to a "burning algorithm" [see *Lindquist et al.*, 1996]. Figure 6 is a two-dimensional illustration of the medial axis behavior of two nodal pores. A throat is defined as a local minimum of the cross-sectional area in a channel, and pores are interconnected by the throat structure. In this study, pore structures of interest are examined using the effective radii of the throats and interconnected pores that are converted from the two nodal pores evaluated, as shown in Figure 7.

3. Experimental Results and Analyses

The evolution in permeability may be attributed to the mechanical creep compaction, the truncation of the contacts by mineral dissolution, the clogging of pore spaces by secondary mineral precipitation onto the

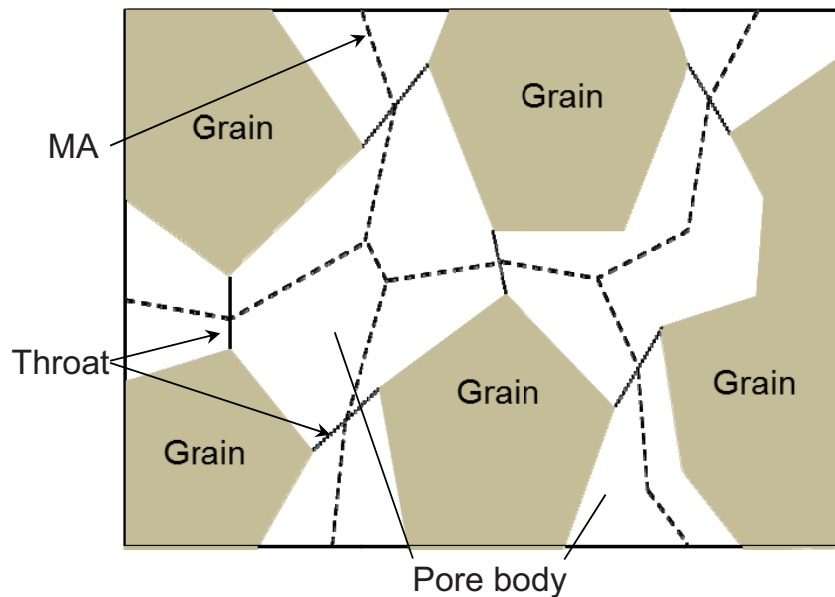


Figure 6. Schematic of pore body and throat defined by medial axis method [Lindquist and Venkataraman, 1999]. MA represents the medial axis for the pore body and throat.

void surfaces and/or by fines resulting from grain crushing, or the convolved behavior of all three phenomena, which should result in a reduction in permeability with time. It may also be attributed to the enlargement of the pore spaces by mineral dissolution from the free surfaces of grains, which should lead to an increase in permeability with time. Notably, the dissolution- and stress-driven compaction by dissolution at the contacts and by the deforming and/or crushing of the contacts, respectively, may be quite difficult to distinguish. The deconvolving of these two mechanisms may not be accomplished simply by measuring the changes in permeability with time, but may be achieved by adding supplementary observations, such as SEM-EDX and X-ray CT. In this study, the aim is to examine the mechanisms of the changes in permeability with time from permeability measurements, together with supplementary observations, analyses of the element concentrations in the effluent fluids, XRF, XRD, SEM-EDX, and X-ray CT with mercury porosimetry.

3.1. Evolution of Permeability

In the case of the intact sandstone samples at 20°C (Figure 8a), the permeability of B-42 starts with $5.14 \times 10^{-15} \text{ m}^2$ and shows slight changes up to the 320th day. Subsequently, the tendency for change increases with time throughout the rest of the experiment; it reaches $1.44 \times 10^{-14} \text{ m}^2$ by the end. Similarly, for sample B-43, the permeability shows a slight oscillation, and then starts increasing with time from the 300th day to the completion of the experiment. The permeability of B-43 is always smaller than that of B-42, which may be due to the higher confining pressure that has been prescribed. In the case of the intact sandstone

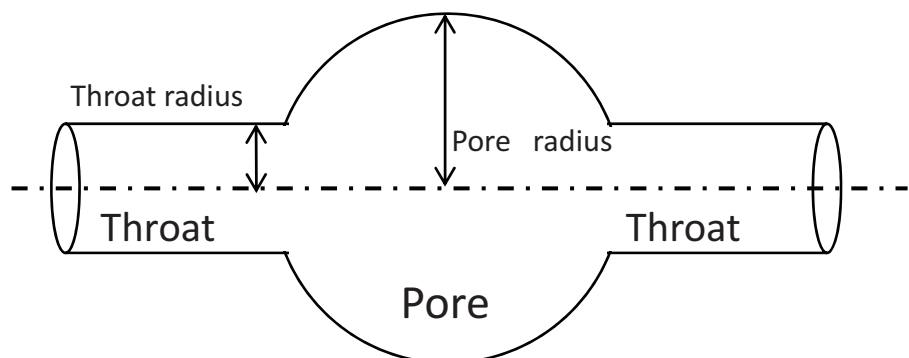


Figure 7. Schematic of pore and throat structures identified using microfocus X-ray CT imaging data.

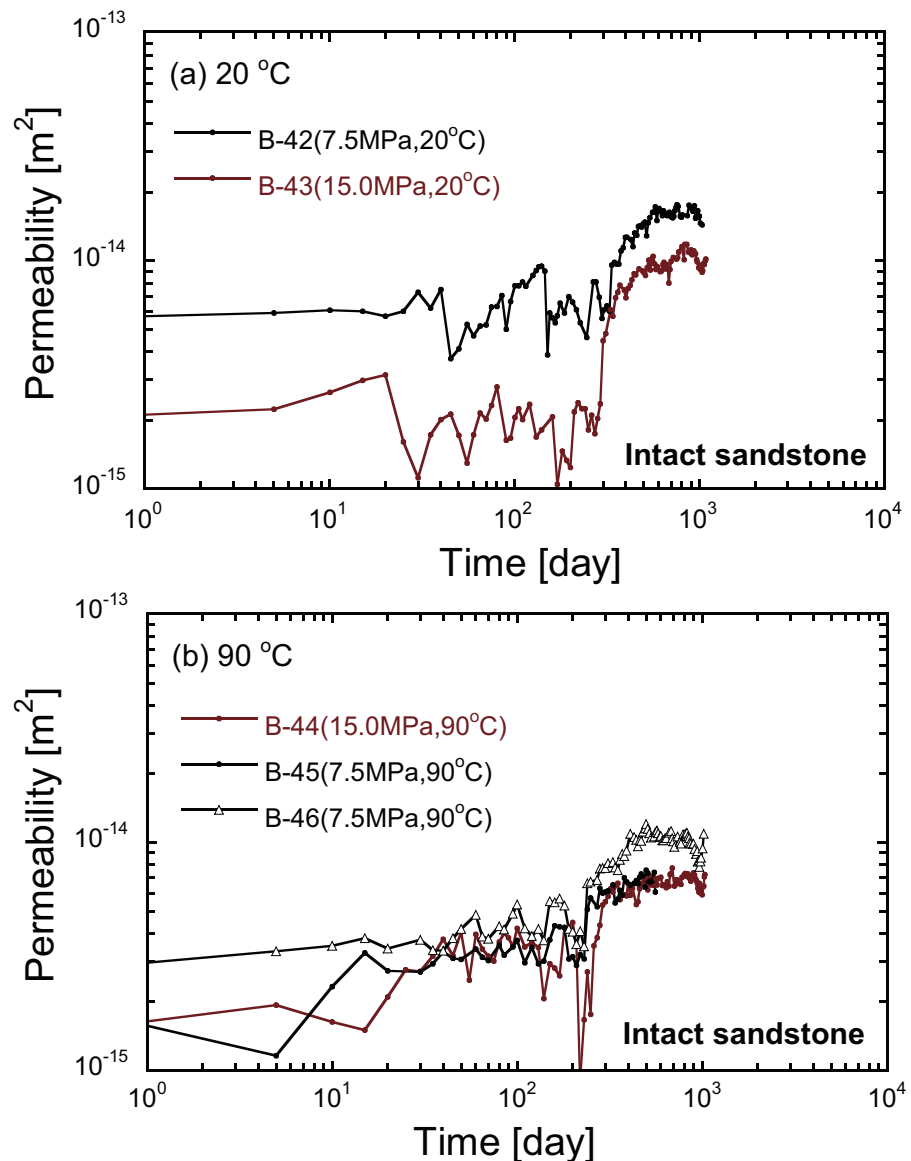


Figure 8. Change in permeability with time in intact sandstone. (a) 20°C and (b) 90°C.

samples at 90°C (Figure 8b), the permeability of samples B-45 and B-46 (i.e., confining pressure of 7.5 MPa) and that of sample B-44 show the same tendency. A subtle discrepancy among them is observed, although the confining pressures that have been prescribed are double. It should be noted that the same boundary conditions were applied to the experiments on samples B-45 and B-46 in order to check the reproducibility of the experiments. As is apparent from Figure 8b, the reproducibility is confirmed. Similar to the experimental results at 20°C (B-42 and B-43), the steady state periods with permeability ranging from 1 to $3 \times 10^{-15} \text{ m}^2$ are followed by periods of an increase in permeability. The timing for the switchover is at around the 250th day, namely, slightly earlier than that for B-42 and B-43. The higher the prescribed temperature, the more soluble the minerals are. Thus, the timing for the switchover in the experiments at 90°C may be advanced. However, when closely comparing the changes in permeability between B-43 and B-44 (Figure 9), no distinct difference is observed, implying that the difference in temperature between 20 and 90°C may not exert a significant influence on the changes in permeability. The dissolution rate constants of quartz, which is the most abundant mineral in Berea sandstone, are evaluated to be 3.14×10^{-13} and 8.82×10^{-11} at 20 and 90°C, respectively [Dove and Crerar, 1990]. The difference in rate constants seems

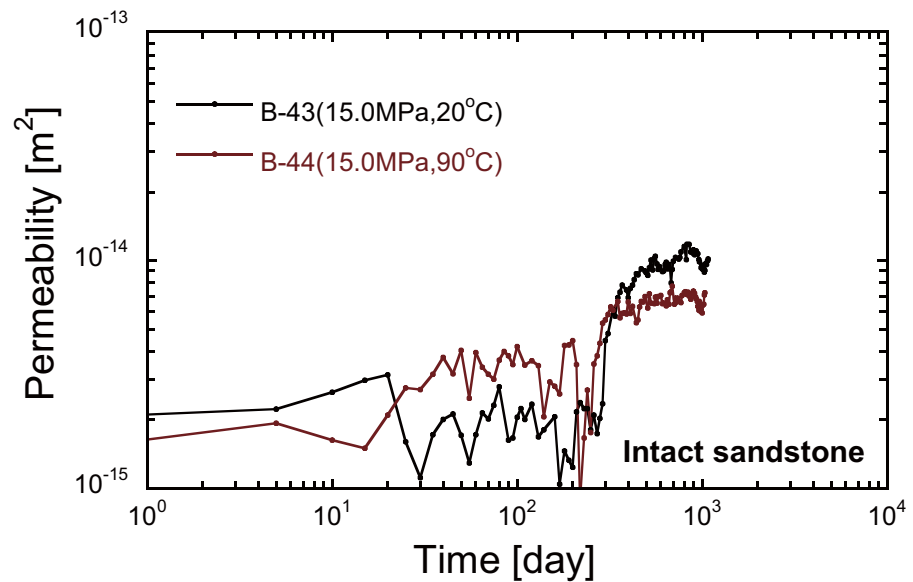


Figure 9. Comparison of change in permeability with time between B-43 and B-44.

significant, but quite a similar phenomenon was indeed observed in this work. In the case of the intact sandstone samples, on the whole, the permeability increases with time after experiencing the steady state period. This is most likely due to the augmentation of pore spaces with time mediated by the mineral dissolution of the free surfaces of the grains.

Next, the results of permeability experiments for the fractured sandstone samples, evaluated by equations (2) and (3), are explained. As is apparent in Figure 10, the permeability in the fractured samples is always more than one hundred times that measured in the intact samples (see Figures 8 and 9), proving that the flow is dominant in the fractures rather than in the matrix. At 20°C (B-47), the permeability decreases monotonically from 5.43×10^{-11} to 6.48×10^{-12} m², 12% relative to the initial value (Figure 10). Such a significant decrease in permeability in the rock fractures, observed under relatively mild stress and temperature conditions, has been previously reported for quartzite [Polak *et al.*, 2003; Yasuhara *et al.*, 2006] and for carbonates [Polak *et al.*, 2004], congruent with the experimental results. At 90°C (B-48), the permeability changes little throughout the experimental period, although it shows a declining trend. This is incongruent with the results reported in the above literature, and may be attributed to the fact that the effects of both fracture gaping (i.e., dissolution of the free surfaces of the grains) and fracture closure (i.e., crushing or dissolution of the grain contacts) counterbalance each other. This theory is still under investigation.

In the fractured mudstone samples, at both 20 and 90°C, the permeability decreases with time (Figure 11). The rate and magnitude of the decrease in permeability are greater at 90°C than at 20°C. In contrast, the permeability decreases little in the experiment on H-5 where nonwetting silicon oil is used as the permeant to inhibit mineral dissolution. Therefore, the reduction observed for H-1 and H-3 should be attributed not to mechanical creep compaction, but to geochemically driven compaction by the mineral dissolution at the contacts and/or to pore clogging induced by mineral reprecipitation. Generally, it was observed that the fracture permeability in both sandstone and mudstone decreased with time, although the rate and magnitude were different among the samples.

3.2. Evolution in Effluent Concentration

In the experiment with B-42, the concentrations show a declining trend with slight fluctuations, but do not change greatly with time throughout the whole experimental period (Figure 12). This tendency is representative of the results for all the sandstone samples. The Ca and Mg concentrations are relatively high compared to the others. This should be attributed to the dissolution of dolomite cements [Dawson *et al.*, 2015], which are more soluble than quartz, the most abundant mineral composing the Berea sandstone.

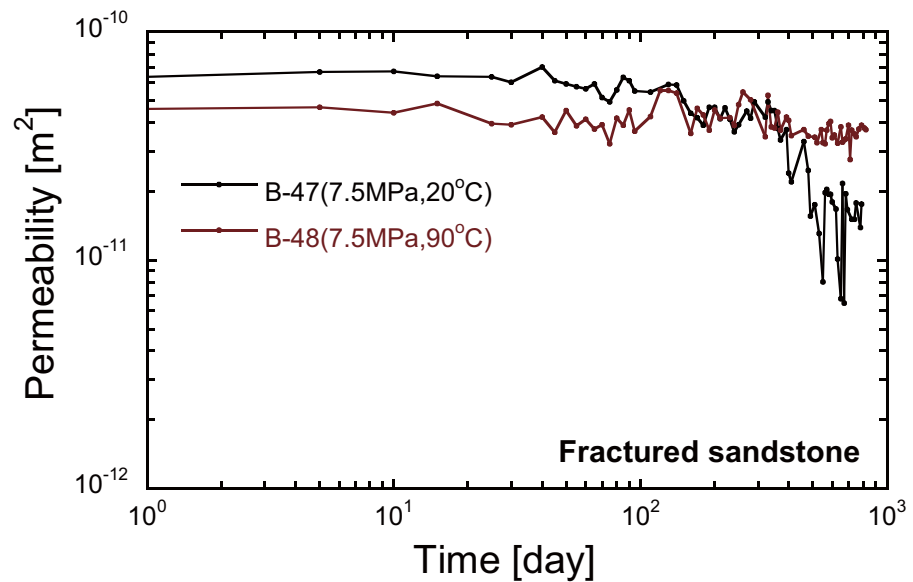


Figure 10. Change in permeability with time in fractured sandstone.

In order to examine the stress and temperature dependence on the measured element concentrations, Si concentrations for all the Berea samples are selected and plotted in Figure 13. In this figure, the circles and rectangles represent the results at 7.5 and 15 MPa, respectively. The black and red-colored symbols show the results at 20 and 90°C, respectively. The closed and open symbols are the results obtained using intact and fractured samples, respectively. As noted in the beginning of this section, all the concentrations decrease with time. However, the rate of decrease is smaller at 90°C than at 20°C. Moreover, the magnitude of the concentrations is always greater at 90°C than at 20°C, which is reasonable. In contrast, the measured concentrations do not show a clear stress dependence. The results at both 7.5 and 15 MPa show quite similar values. Interestingly, the concentrations in the fractured samples (B-47 and B-48) also show a similar trend, both quantitatively and qualitatively, as compared with those in the intact samples (B-42, B-43, B-44, B-45, and B-46), indicating that the existence of a fracture may exert little influence on the evolution of mineral dissolution. It is concluded for the concentration measurements in the Berea sandstone that the confining pressures adopted in this work (i.e., 7.5 and 15 MPa) may have little influence on the change in the amount of mineral dissolution and that the prescribed temperature may regulate the mineral dissolution. At least it can be said that the temperature effect is greater than the stress effect.

Next, the concentrations measured in the Horonobe mudstone are explained. Similar to the measurements apparent in the sandstone samples, the measured concentrations gradually decrease with time and show greater values at 90°C than at 20°C (Figure 14). Notably, the Na and Cl concentrations are relatively high. This most likely can be attributed to the dissolution of the soluble NaCl included within the matrix pores.

The dissolved mass in the solutions should originate from both the contacting areas and the free walls within the pore spaces. If the effect of the free-face dissolution dominates over that acting on the contacting areas, the permeability should increase with time, which is compatible with the measurements in the intact sandstone samples. In contrast, if the effect of the dissolution at the contacts prevails over the free-face dissolution, the permeability should decrease with time. This interpretation is supported by the measurements in the fractured sandstone and mudstone samples. As is apparent, the upper and lower walls of a fracture are propped by asperity contacts. Therefore, the truncation of the propping asperities by dissolution in the fractured media may result in the decrease in permeability with time.

3.3. Petrographic Analyses Using SEM-EDX, XRD, and XRF

The experiments on B-42 (7.5 MPa and 20°C) and B-45 (7.5 MPa and 90°C) were halted, and the samples were taken out of the pressure cell to examine the petrographic changes by comparing the pre and postexperimental samples by means of SEM-EDX, XRD, and XRF. The other samples were still within pressure cells

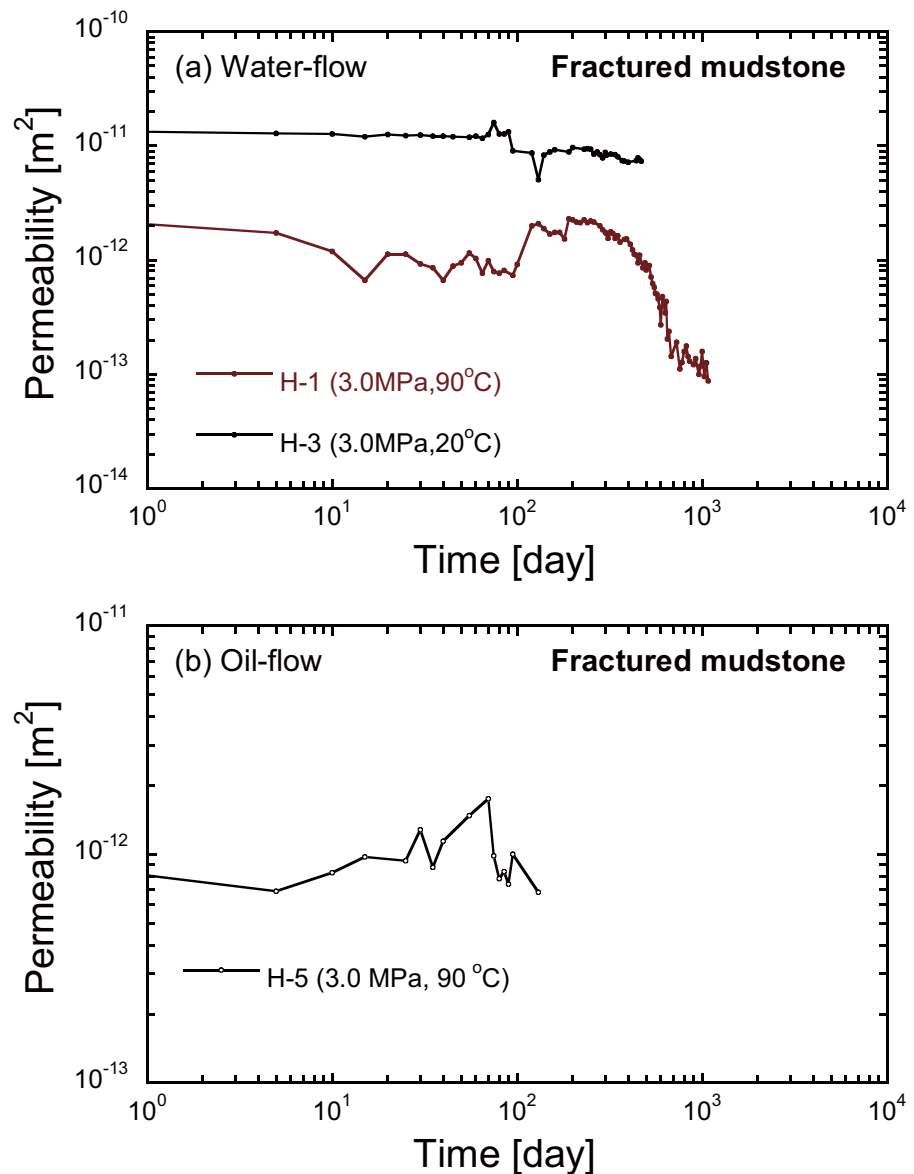


Figure 11. Change in permeability with time in fractured mudstone. (a) Water flow experiments and (b) oil flow experiment.

and the experiments were continuously conducted. The experimental durations for B-42 and B-45 were 1015 and 566 days, respectively. The dimensions and the P wave velocity of the two samples were measured in a longitudinal direction before and after the experiments. The results are shown in Table 3. The dimensions of B-42 changed little during the experiments, while those of B-45 contracted slightly in the longitudinal direction. The contraction may be attributed to the truncation of the grain contacts, induced by the pressure solution, that are more active at higher temperatures [e.g., Rutter, 1983; Bjørkum, 1996; Revil, 1999]. However, further analyses are required to clarify this hypothesis. Notably, the measured P wave velocity is lower in the postexperimental samples than in the preexperimental samples for both B-42 and B-45. This reduction should be attributed to the dominant effect of the free-face dissolution of the minerals, leading to the augmentation of pore spaces, and is congruent with the increase in permeability with time observed in the flow-through experiments (Figure 8).

When closely observing the postexperimental samples, red-colored secondary precipitates were found that were not observed in the preexperimental samples, as seen in Figure 15, striped patterns, composed of red and white layers, clearly extend along the bedding plane. Figure 16a shows a close view of such red precipitates. The SEM-

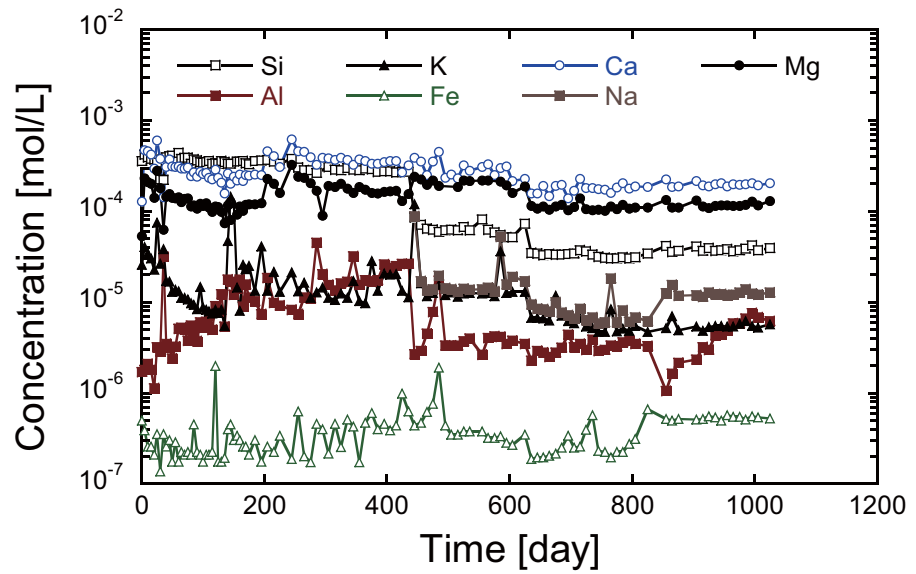


Figure 12. Evolution of effluent element concentrations of Si, Al, K, Fe, Ca, Na, and Mg in experiment on B-42. They are measured using ICP-AES.

EDX analysis revealed that the red precipitates are dominated by Mg, Ca, and Fe (Figures 16b–16d) and are interpreted to consist of a mixture of dolomite ($\text{CaMg}(\text{CO}_3)_2$) and siderite (FeCO_3). The SEM image and the elemental maps suggest that the dolomite precipitated first within the pore spaces, followed by the siderite precipitation which eventually filled in the pores completely. Siderite is commonly found in hydrothermal veins and is also known to occur frequently as a representative diagenetic mineral. Relatively pure siderite was observed in these experiments because deionized water was used as the permeant [Mozley, 1989].

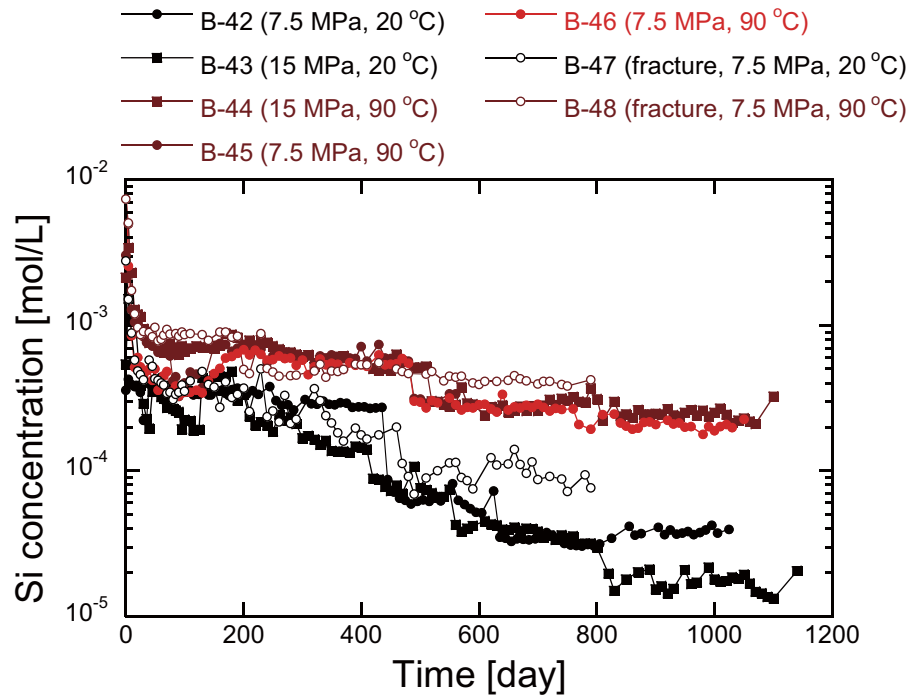


Figure 13. Evolution of Si concentrations in experiments on B-42, B-43, B-44, B-45, B-46, B-47, and B-48. The circles and rectangles represent the results at 7.5 and 15 MPa, respectively. The black and red-colored symbols represent the results at 20 and 90°C, respectively. The closed and open symbols show the results obtained using intact and fractured samples, respectively.

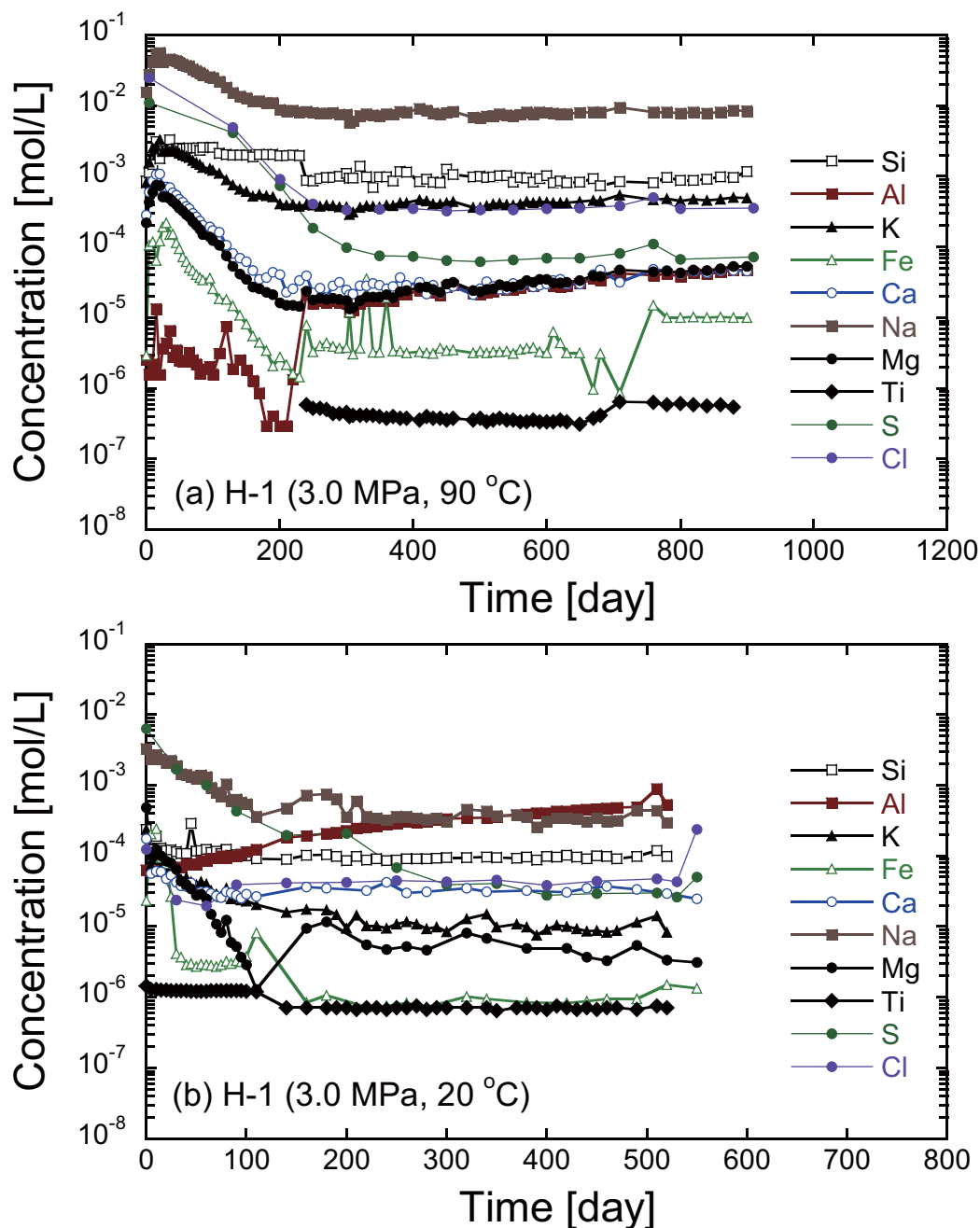


Figure 14. Evolution of effluent element concentrations of Si, Al, K, Fe, Ca, Na, Mg, S, and Cl in experiments on (a) H-1 and (b) H-3. They are measured using ICP-AES and IC.

The mineral composition of the postexperimental samples, B-42 and B-45, was determined by XRD, as shown in Figure 17. The only difference in mineral composition between the pre and postexperimental samples is the illite (see Figure 2 as a reference), which commonly occurs as an alteration product of feldspar in weathering and hydrothermal environments [e.g., Demange, 2012]. The relatively high temperature of 90°C and the long-term hold duration are likely to have accelerated the alteration of feldspar to illite. However, siderite, identified by the SEM-EDX analysis, was not detected by the XRD measurement because of its small volume fraction. This result implies that the precipitation of siderite may not influence the reduction in permeability mediated by the local clogging of the precipitates because the net permeability indeed increased with time.

The element composition of the pre and postexperimental samples was determined by XRF, as shown in Table 4. The same trends for B-42 and B-45 are the increase in Si and the decrease in the amount of Ca and

Table 3. Dimensions and *P* Wave Velocities of Pre- and Postexperimental Samples

Sample	Confining Pressure (MPa)	Temperature (°C)	Experimental Duration (day)	Diameter (mm) ^a	Height (mm) ^a	<i>P</i> Wave Velocity (km/s) ^a
B-42	7.5	20	1015	Pre 30.00	60.00	2.37
				Post 30.05	60.00	2.26
B-45	7.5	90	566	Pre 30.00	60.00	2.36
				Post 30.00	59.80	2.25

^aThe upper and lower values represent the results before and after the experiments, respectively.

Mg as compared with the results for B-00 (the preexperimental sample). The reduction in Ca and Mg implies the dissolution of dolomite, which is reasonable and compatible with the measured Ca and Mg concentrations, that are relatively high, and comparable to the Si concentrations (Figure 12). The augmentation of pore spaces with time may be due mainly to the dolomite dissolution.

3.4. Observations of Micropores Using Microfocus X-ray CT

The rock samples, B-42 (7.5 MPa and 20°C) and B-45 (7.5 MPa and 90°C), were also investigated by the microfocus X-ray CT to examine the evolution of pore structures by comparing pre and postexperimental samples. A CT image and the extracted pore structures of B-45 are shown as an example in Figure 18. The

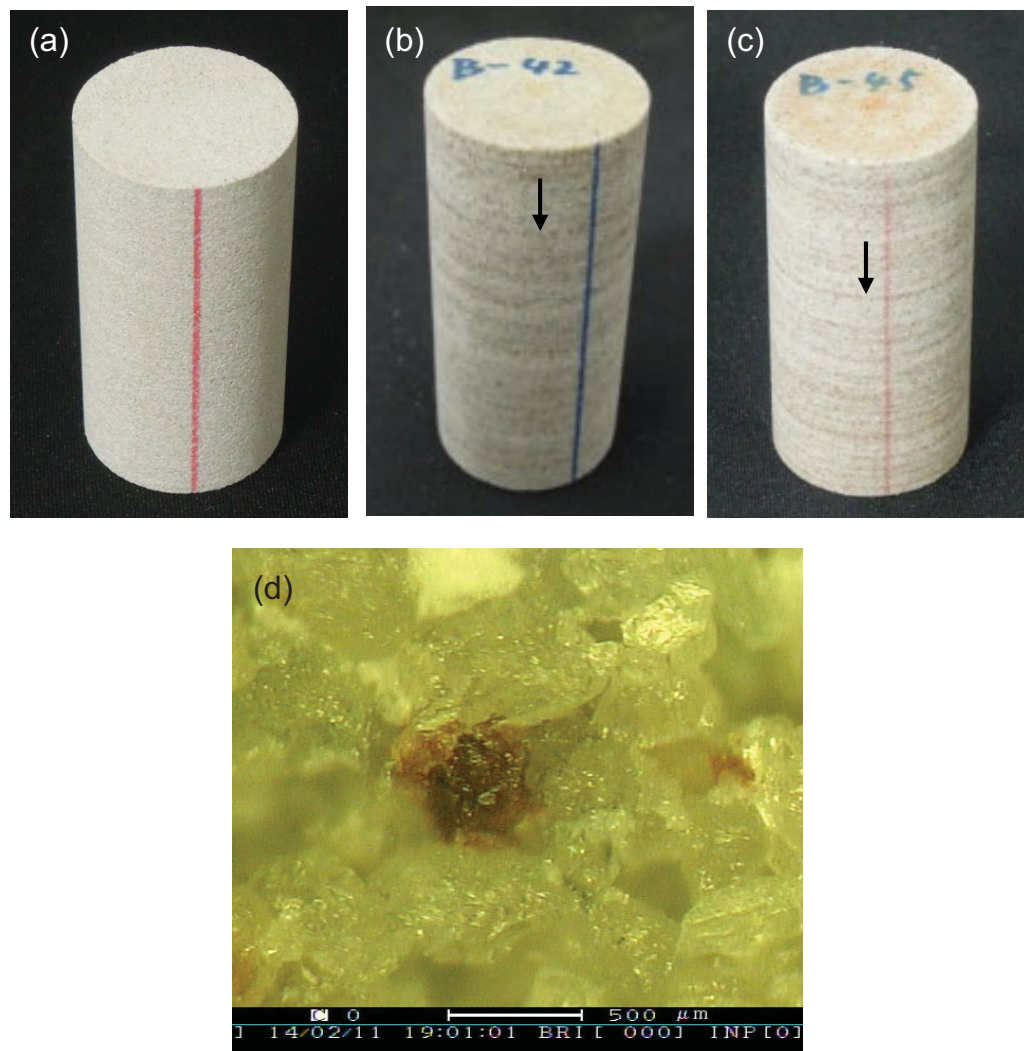


Figure 15. (a) Preexperimental sample (borrowed from Figure 1a) and postexperimental samples (b) B-42, (c) B-45, and (d) close view of red-colored precipitates, shown using arrows in Figures 15b and 15c, by optical microscope.

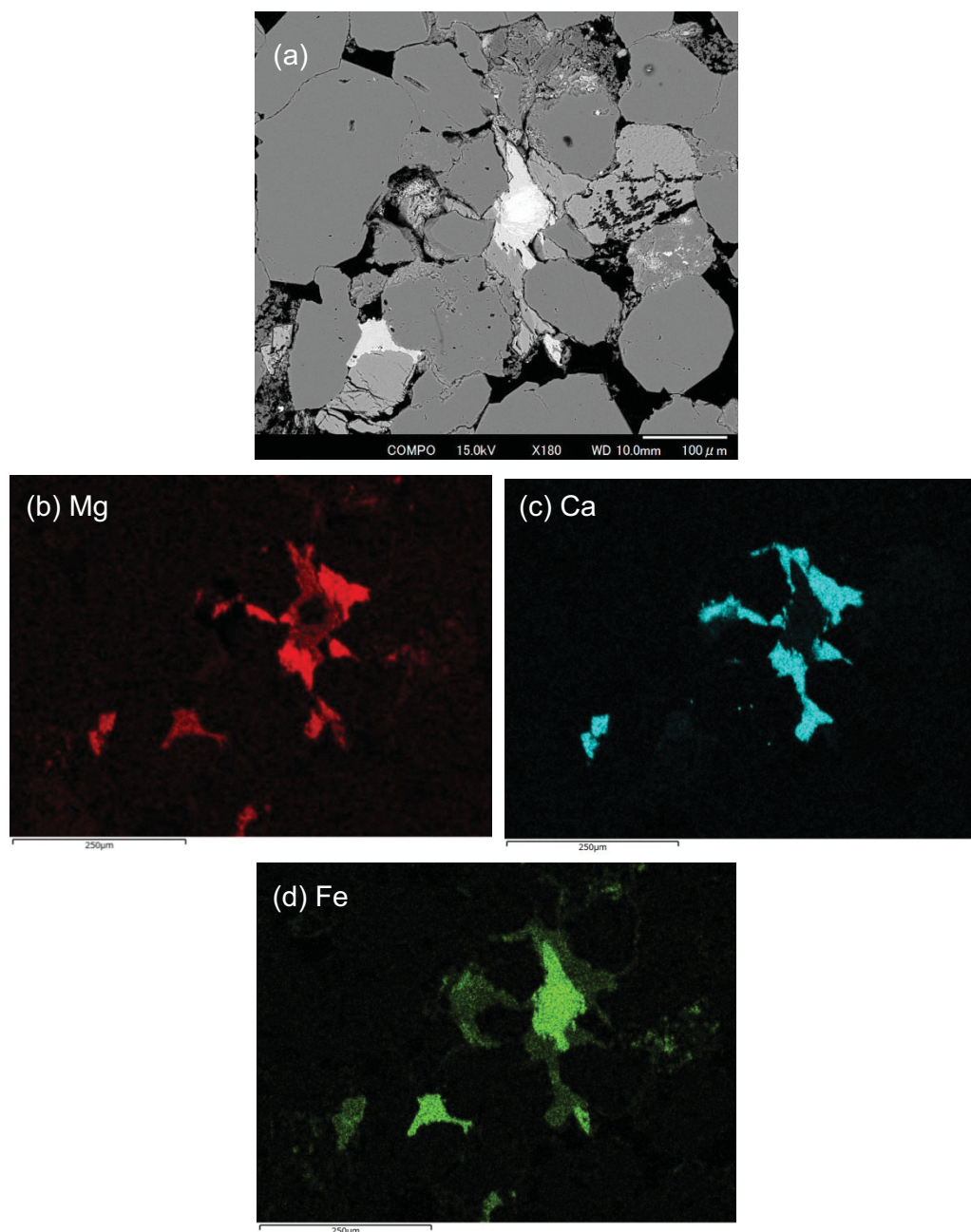


Figure 16. Postexperimental SEM-EDX observation in B-42. (a) SEM (backscattered electron) image, (b) Mg map, (c) Ca map, and (d) Fe map.

differences in the relative frequency of the effective pore and throat radii between the pre and postexperimental samples, B-42 and B-45, are shown in Figure 19. As is apparent, the pores with a radius ranging from 10 to 60 μm decreased, while those with a diameter of more than 60 μm increased for both B-42 and B-45. Similarly, the throats with a radius ranging from 5 to 25 μm decreased, while those with a diameter of more than 60 μm increased for B-42, although such a distinct difference in throat radii was not observed for B-45. The decrease in smaller pores and the increase in larger pores should result in an increase in permeability. This supports the permeability measurements shown in Figure 8.

3.5. Discussion

We have observed interesting results in the long-term permeability change—the observed permeability in the intact rock samples generally increased with time, while that in the fractured rock samples decreased

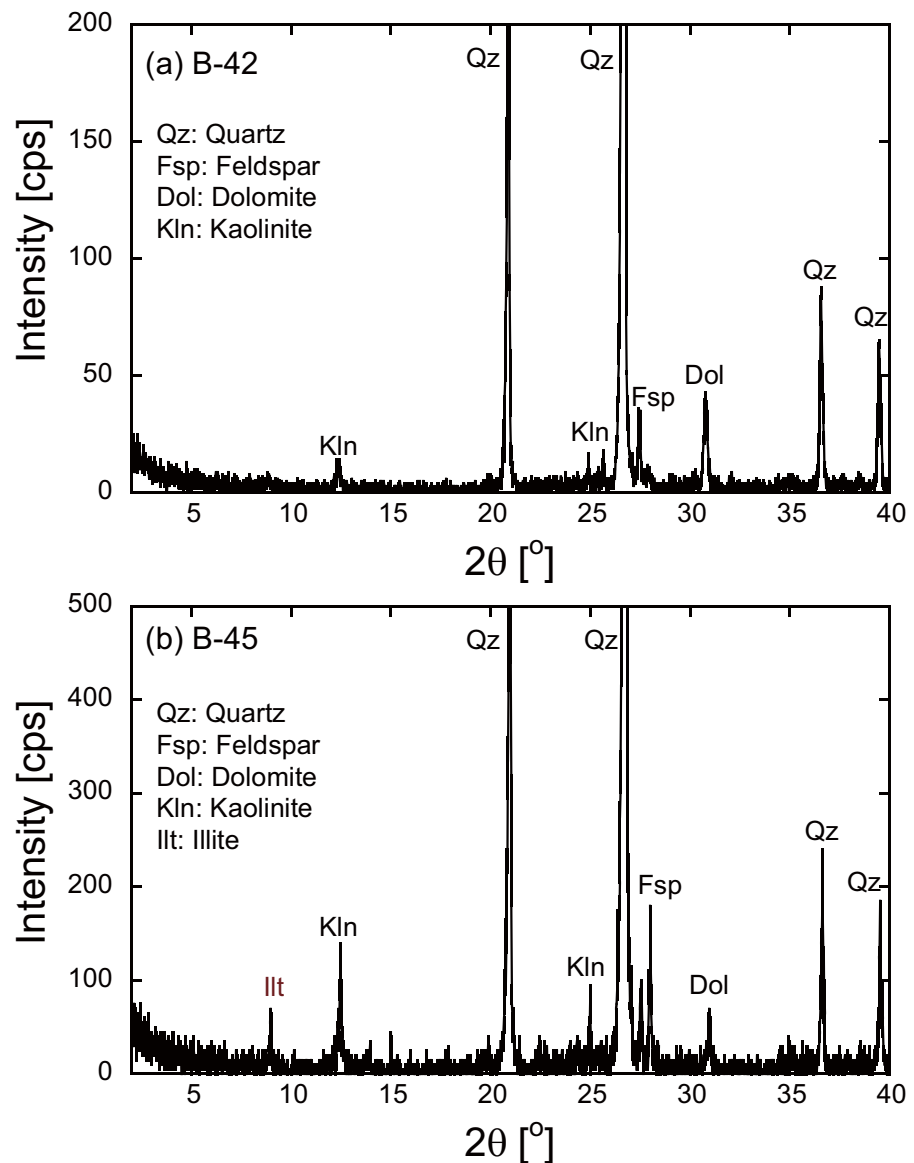


Figure 17. Mineral composition of rock samples determined by XRD. (a) B-42 and (b) B-45. Illite was observed in B-45, which is the only difference between the pre and the postexperiments.

with time. To examine the mechanisms of the change in permeability, the dimensionless Damkohler number, Da_l , at the sample scale was evaluated by following *Salehikhoo et al.* [2013]. This number describes the effect of advection relative to that of mineral dissolution at the sample scale, given by,

$$Da_l = \frac{\tau_{adv}}{\tau_{rxn}} = \frac{\frac{l}{\bar{v}}}{\frac{V_p C_{eq}}{RA_T}} = \frac{L RA_T}{\bar{v} V_p C_{eq}}, \quad (4)$$

where τ_{adv} is the characteristic time scale for advection (s) and τ_{rxn} is the characteristic time scale for dissolution (s). The characteristic time scale for advection is the residence time of the fluid in the rock sample, defined as $\tau_{adv} = \frac{l}{\bar{v}}$, where \bar{v} is the average flow velocity (m s^{-1}). In this study, the pore water within the rock samples was replaced with fresh deionized water at the interval of 5 or 10 days, and the length of the rock samples was 60 mm. Therefore, the average flow velocity may be defined as $1.4 \times 10^{-7} \text{ m s}^{-1}$, as a first-order approximation. The characteristic time scale for the dissolution is the time that it takes to reach equilibrium in the entire rock sample; it is defined as $\tau_{rxn} = \frac{V_p C_{eq}}{RA_T}$, where V_p is the total pore volume of the rock sample (m^3), C_{eq} is the equilibrium concentration (mol m^{-3}), R is the sample scale dissolution rate ($\text{mol m}^{-2} \text{ s}^{-1}$), and A_T is the total

Table 4. Composition of Pre and Postexperimental Samples

Oxide	Results (wt %)		
	B-00	B-42	B-45
SiO ₂	82.6	88.2	83.3
Al ₂ O ₃	9.88	6.66	10.1
Fe ₂ O ₃	2.13	1.51	2.04
K ₂ O	1.97	1.68	2.49
CaO	1.66	0.773	0.518
MgO	0.973	0.671	0.662
TiO ₂	0.633	0.383	0.744
Others	0.154	0.150	0.175

surface area (m²) [Salehikhoo et al., 2013]. Both the Berea sandstone and the Horonobe mudstone are composed mainly of silica (Figure 2). We assume that quartz is the representative mineral that may control the overall dissolution occurring in the rock samples, and that the whole system is far from equilibrium. The effluent element concentrations measured in the sandstone sample, B-42, as shown in Figure 12, indicate that the dolomite cements may have contributed to the change in permeability, but the effect is not considered here for simplicity. Consequently, the parameters for C_{eq} and R can be evaluated using the solubility of amorphous silica in water [Fournier and Rowe, 1977] and the dissolution rate constants of quartz [Tester et al., 1994], respectively.

For the intact sandstone samples, the term of $\frac{A_r}{V_p}$ in equation (4), is calculated by assuming that the sandstone samples are composed of closely packed spheres, defined as $\frac{A_r}{V_p} = \frac{12.57r^2}{1.47r^3}$ [Graton and Fraser, 1935], where r is the mean radius of grains composing the sandstone, namely, $\sim 100 \mu\text{m}$. For the fractured sandstone and mudstone samples, the values of τ_{adv} , C_{eq} , and R are the same as those used for the calculations of the intact sandstone samples. The term of $\frac{A_r}{V_p}$ is calculated by assuming that the fractures contain smooth, flat surfaces without any roughness, defined as $\frac{A_r}{V_p} = \frac{2}{w^2}$, where w is the average fracture aperture, for which the hydraulic aperture $\langle b \rangle$, shown in equation (2), is substituted in this study. Actually, the initial values for the hydraulic aperture evaluated from the permeability experiments are used to calculate $\frac{A_r}{V_p}$. Finally, all the parameter values and the evaluated D_{ai} are summarized in Table 5.

In both the intact and the fractured rock samples (i.e., B-42, B-43, B-47, and H-3), D_{ai} shows similar values when the temperatures are equal. At 20°C, D_{ai} is relatively close to unity, meaning that the effects of advection and dissolution balance each other and dissolution may locally reach a steady state or equilibrium between injections of fresh deionized water, while at 90°C (i.e., B-44, B-45, B-46, B-48, and H-1), D_{ai} is 3 orders of magnitude greater than that at 20°C, meaning that the dissolution process should more quickly reach a steady state or equilibrium in a larger domain of the rock samples. After all, the system is more or less dissolution-limited at both temperatures; and thus, the permeability changes in the intact sandstone samples, B-42, B-43, B-44, B-45, and B-46, show a similar trend even at different temperatures. Dissolution occurs on the free surfaces of grains and the cements, and the dissolved materials are flushed out of the rock samples during each permeability experiment. Subsequently, the pore volume gradually increases and it takes several hundred days to observe a measurable increase in permeability. Therefore, unless the pore water is replaced with freshwater, the permeability may not change with time, which should be confirmed by conducting circulating-flow experiments.

In the fractured samples of sandstone and mudstone, B-47, B-48, H-1, and H-3, D_{ai} is the same as that of the intact samples. However, the observed behavior is totally different—the permeability decreased with time. This is obviously due to chemo-mechanical compaction and/or the local precipitation of secondary minerals. As described in section 3.3, many secondary minerals were not observed from the SEM-EDX and XRD analyses, and the reprecipitation may not have exerted a significant influence on the permeability reduction. Therefore,

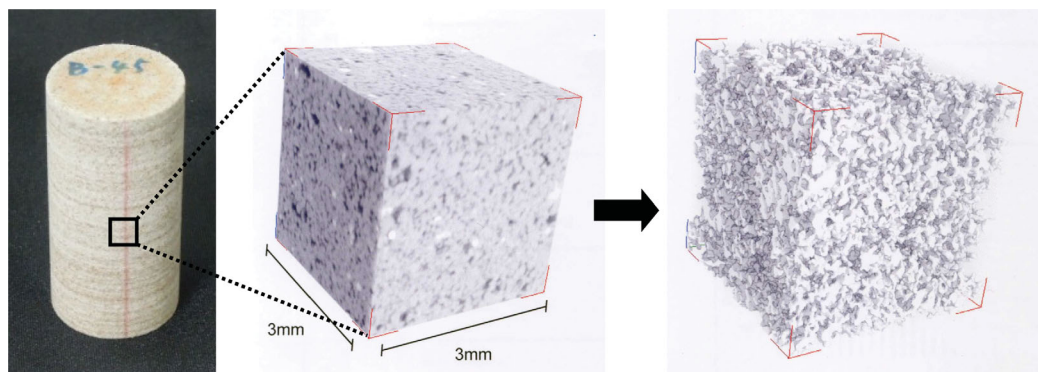


Figure 18. Schematic procedure of extraction of micropores using microfocus X-ray CT. A 3 mm cube is imaged in the middle of the rock sample and pore structures are extracted.

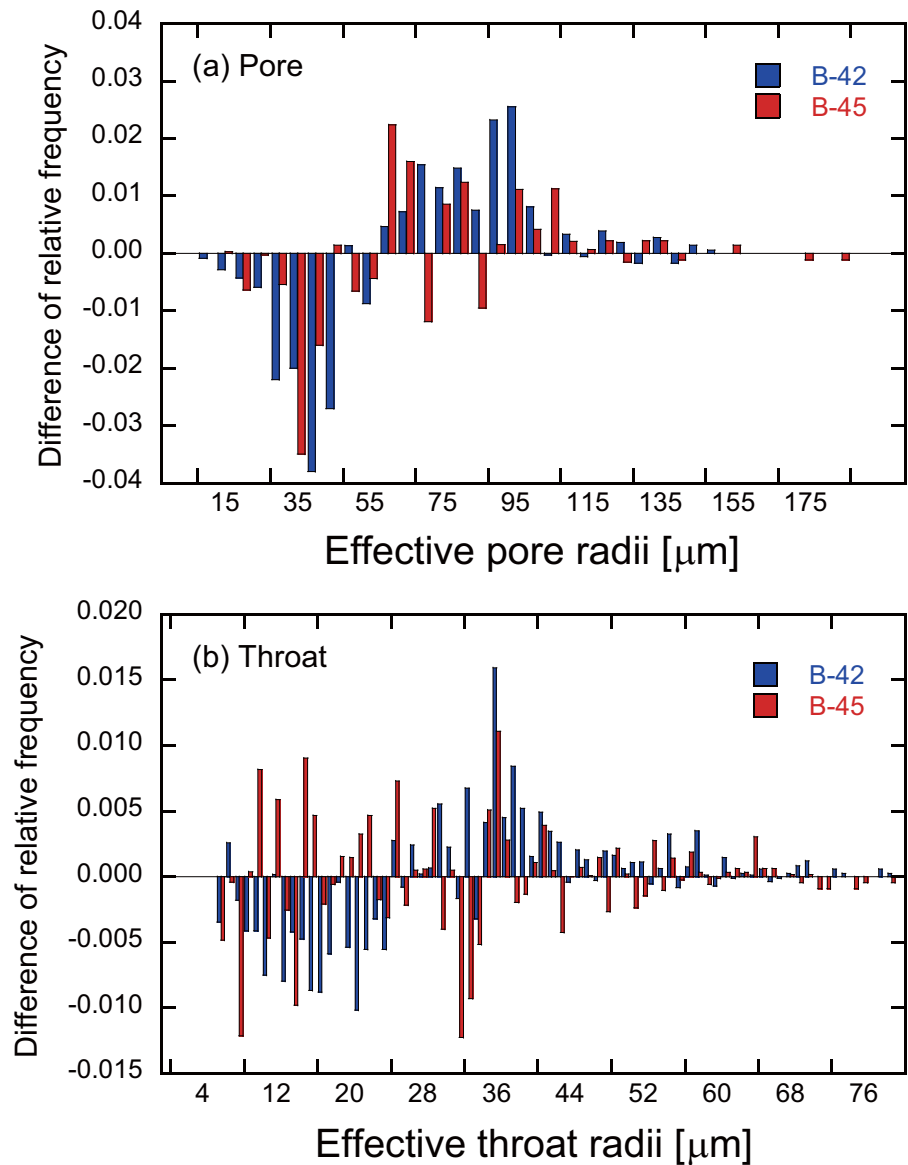


Figure 19. Difference in relative frequency distribution between pre and postexperimental samples. (a) Effective pore radii and (b) effective throat radii.

the observed reduction in permeability may be attributed to geochemically driven compaction by the mineral dissolution. Although D_{ol} was evaluated in this section, we should note that it is difficult to show clearly deterministic interpretations/conclusions for the permeability changes observed in all the samples.

The contribution of net dissolution, measured as the effluent element concentrations, to the permeability changes in the intact sandstone samples, B-42, B-43, B-44, B-45, and B-46, may be evaluated by calculating the net dissolution mass flux flowing out of the samples at a given time, as,

$$\dot{M}(t) \approx Q \sum_i C_i(t), \quad (5)$$

where $\dot{M}(t)$ is the net dissolution mass flux (kg s^{-1}), Q is the flow rate ($\text{m}^3 \text{s}^{-1}$) ($Q = 8 \text{ mL}/10 \text{ days}$), and $C_i(t)$ is the concentration of oxides i (kg m^{-3}) ($i = \text{SiO}_2, 1/2(\text{Al}_2\text{O}_3), \text{FeO}, 1/2(\text{K}_2\text{O}), \text{CaO}, \text{MgO}, 1/2(\text{Na}_2\text{O})$). The measured concentrations were originally obtained as those of the elements (i.e., Si, Al, Fe, K, Ca, and Mg) in units of mg L^{-1} , and then those of the oxides were computed. Subsequently, the porosity change due to the net dissolution can be obtained by

Table 5. Parameters Used in Equation (4) and Obtained Damkohler Numbers

Sample	\bar{v} (m s ⁻¹)	C_{eq}^a (mol m ⁻³)	R^a (mol m ⁻² s ⁻¹)	$\frac{A_r}{V_p}$ (m ⁻¹)	τ_{adv} (s)	τ_{rxn} (s)	D_{dl} (-)
B-42 (20°C, intact)	1.4×10^{-7}	4.1×10^{-3}	6.6×10^{-14}	8.6×10^4	3.5×10^5	7.2×10^5	0.49
B-43 (20°C, intact)	1.4×10^{-7}	4.1×10^{-3}	6.6×10^{-14}	8.6×10^4	3.5×10^5	7.2×10^5	0.49
B-44 (90°C, intact)	1.4×10^{-7}	1.4×10^{-2}	5.9×10^{-10}	8.6×10^4	3.5×10^5	2.8×10^2	1.3×10^3
B-45 (90°C, intact)	1.4×10^{-7}	1.4×10^{-2}	5.9×10^{-10}	8.6×10^4	3.5×10^5	2.8×10^2	1.3×10^3
B-46 (90°C, intact)	1.4×10^{-7}	1.4×10^{-2}	5.9×10^{-10}	8.6×10^4	3.5×10^5	2.8×10^2	1.3×10^3
B-47 (20°C, fracture)	1.4×10^{-7}	4.1×10^{-3}	6.6×10^{-14}	7.8×10^4	3.5×10^5	8.0×10^5	0.44
B-48 (90°C, fracture)	1.4×10^{-7}	1.4×10^{-2}	5.9×10^{-10}	8.8×10^4	3.5×10^5	2.7×10^2	1.3×10^3
H-1 (90°C, fracture)	1.4×10^{-7}	1.4×10^{-2}	5.9×10^{-10}	4.7×10^5	3.5×10^5	5.0×10^1	7.0×10^3
H-3 (20°C, fracture)	1.4×10^{-7}	4.1×10^{-3}	6.6×10^{-14}	2.6×10^5	3.5×10^5	2.4×10^5	1.5

^a C_{eq} and R are evaluated by following Fournier and Rowe [1977] and Tester et al. [1994], respectively.

$$\phi(t) = \phi_i + \frac{1}{V_t} \sum \frac{\dot{M}(t)}{\rho_g} \Delta t, \quad (6)$$

where $\phi(t)$ is the porosity at a given time (-), ϕ_i is the initial porosity (-) ($\phi_i = 0.17$), V_t is the total sample volume (m³) ($V_t = 4.2 \times 10^{-5}$ m³), and ρ_g is the grain density (kg m⁻³) ($\rho_g = 2700$ kg m⁻³). Once the porosity at a given time is evaluated, the change in permeability may be evaluated using the Kozeny-Carman equation [Bear, 1972], as

$$k(t) = k_i \frac{(1 - \phi_i)^2}{(1 - \phi)^2} \left(\frac{\phi}{\phi_i} \right)^3, \quad (7)$$

where $k(t)$ is the permeability at a given time and k_i is the initial permeability. Thus, the term of $\frac{k(t)}{k_i}$ represents the permeability normalized by the initial permeability. The normalized permeability, observed in the experiments and predicted by following the above procedure, is compared in Figure 20. As is apparent, the predicted normalized permeability changes little with time. Actually, the increase in permeability for samples B-42 (20°C) and B-46 (90°C) is only 1% relative to the initial permeability—the increase for B-46 is slightly higher than that for B-42, which is quite reasonable because the higher temperature gives more mineral dissolution. This surprising mismatch between measurements and predictions implies the formation of preferential flow paths, like wormholes, which were not clarified in the microfocus X-ray CT observations. Conducting flow simulations using the 3-D representation of the pore structures obtained from the CT should be the next task to elucidate the greater increase in the measured permeability.

Related to the above discussion, the contribution of net dissolution to the permeability changes in the fractured sandstone and mudstone samples, B-47, B-48, H-1, and H-3, may also be evaluated in a similar manner. The net dissolution mass flux is assumed to be the sum of the fluxes originating from the contact asperities and the free surfaces within the fractures, that is,

$$\dot{M} = \dot{M}_C \cdot r_C + \dot{M}_F \cdot r_F, \quad (8)$$

where r_C and r_F are ratios of the dissolution mass fluxes sourced from the contact areas and the free surface areas over the total mass efflux, respectively, which results in $r_C + r_F = 1$, and represents the relative contribution to the net dissolution mass flux sourced from either the contact areas or the free surfaces. The dissolution at the contact areas and the free surfaces should result in the decrease and increase in permeability, respectively. Therefore, the rates of the changes in mechanical aperture, induced by the dissolution at the contact areas and the free surfaces, may be defined by

$$\dot{b}_C = -(1 - R_C) \frac{\dot{M}_C r_C}{\rho_r A_f R_C}, \quad (9)$$

$$\dot{b}_F = \frac{\dot{M}_F r_F}{\rho_r A_f}, \quad (10)$$

where \dot{b}_C and \dot{b}_F are the rates of the changes in the mechanical aperture induced by the dissolution at the contact areas and the free surfaces, respectively. ρ_r is the dry bulk density of the rocks (kg m⁻³) (2070 kg m⁻³ for Berea sandstone and 1700 kg m⁻³ for Horonobe mudstone). Finally, the rate of the average fracture aperture change, \dot{b} , is defined as

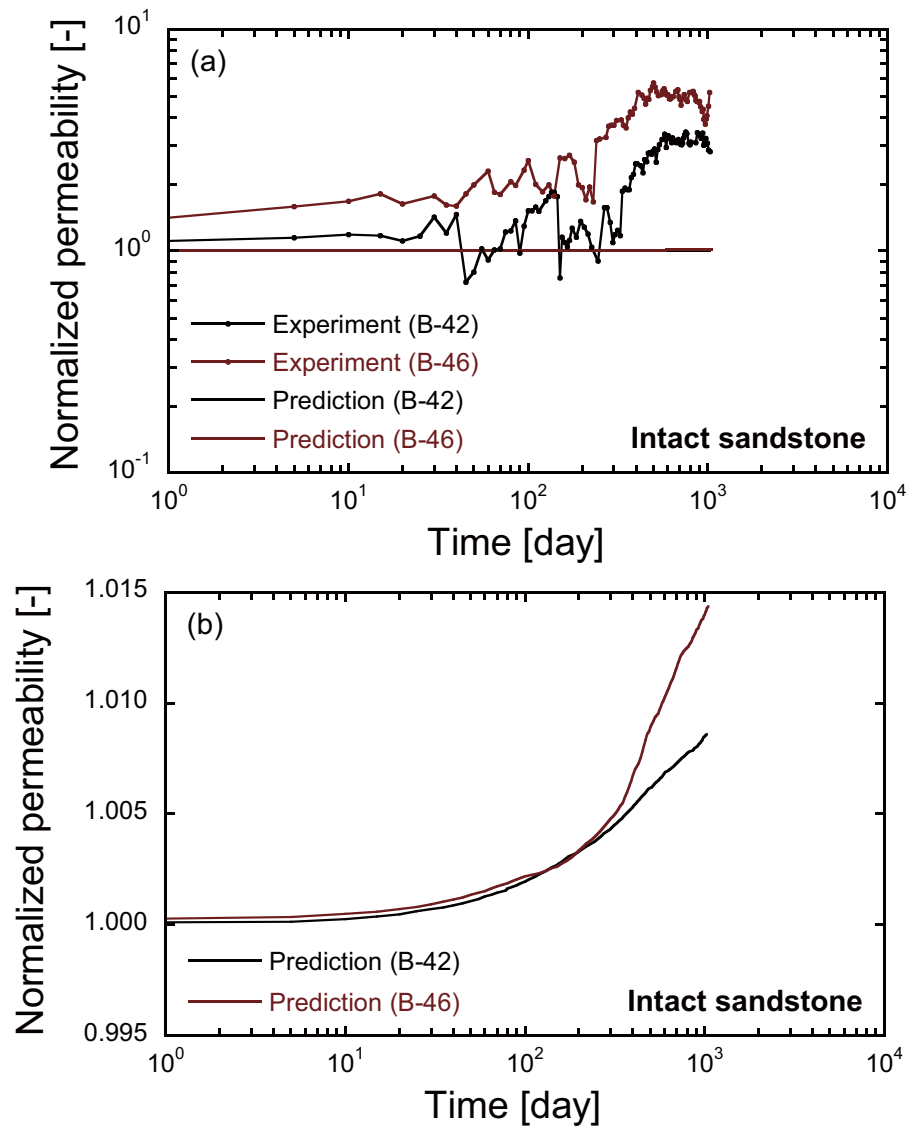


Figure 20. Comparison of normalized permeability between experiments and predictions. (a) Both of experiments and predictions, and (b) close-up view of predictions. The normalized permeability predicted few changes with time.

$$\begin{aligned} \dot{b} &= \dot{b}_c + \dot{b}_f \\ &= \frac{\dot{M}(1-R_c)}{\rho_r A_f} \left(-\frac{r_c}{R_c} + \frac{r_f}{1-R_c} \right), \end{aligned} \quad (11)$$

where R_c is the contact area ratio. Note that although the mechanical aperture predicted here and the hydraulic aperture evaluated from equation (2) may not be equivalent [e.g., Piggott and Elsworth, 1993], calculating them as equivalent is reasonable to a first-order approximation. Varying the unmeasured fractional contact area in the range from 1 to 40%, the rates of aperture reduction, \dot{b} , in equation (11) can be evaluated with the different rates of \dot{b}_c and \dot{b}_f , together with that recovered from the hydraulic measurements changing with time (Figure 21). The predicted \dot{b} decreases with the increase in r_f , which is quite reasonable because the increasing r_f represents the augmenting of the contribution of the free-face dissolution. For samples B-47, B-48, and H-3, the predictions, in the range from 10^{-11} to 10^{-13} m/s, are close to the rates evaluated from the hydraulic measurements. This agreement leads to the conclusion that the dissolution at the contact areas mainly contributes to the observed response. For sample H-1, the predictions in the range from 10^{-10} to 10^{-12} m/s are slightly higher than the measurements. This mismatch may be the result of

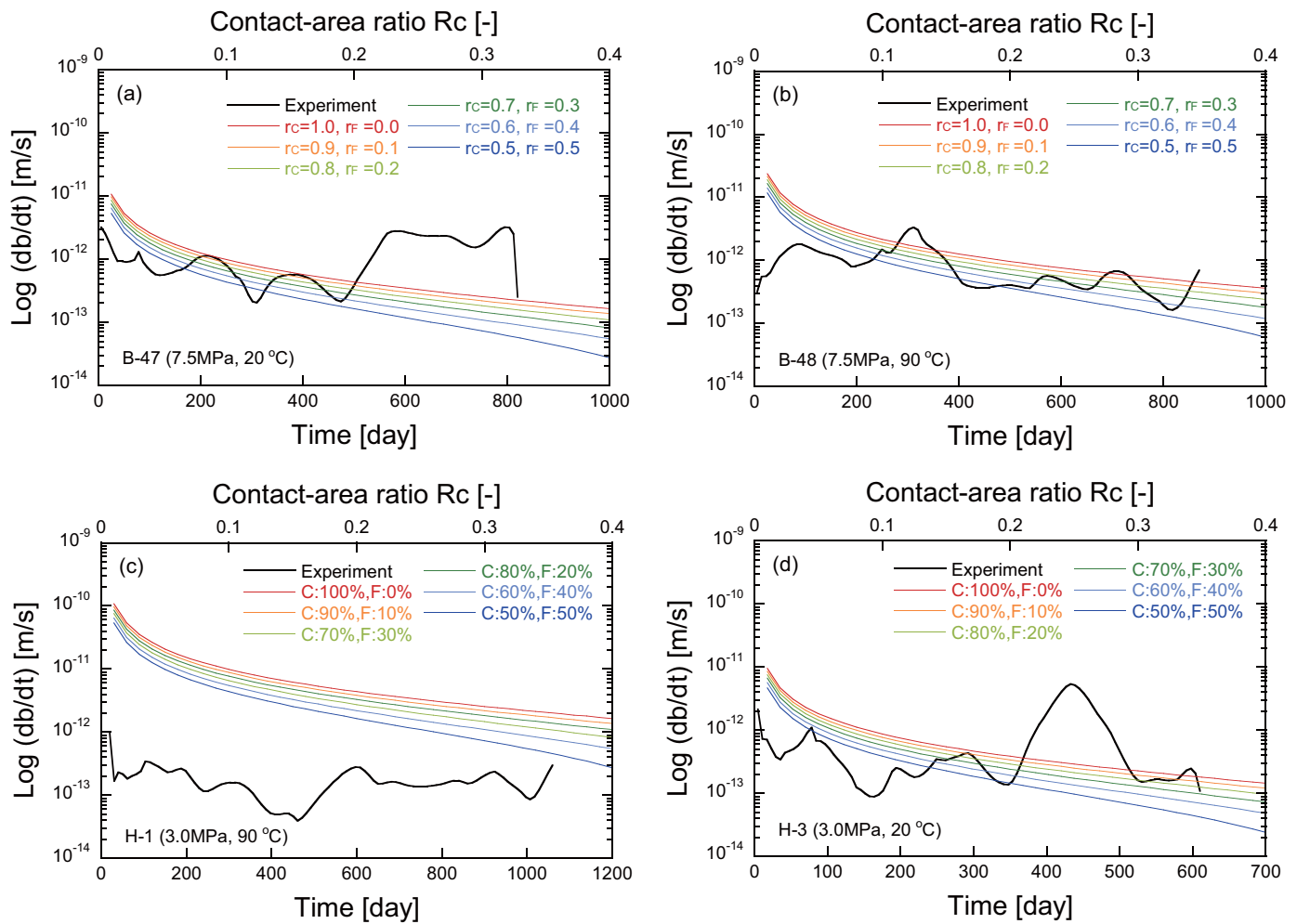


Figure 21. Comparison of rate of aperture change between experiments and predictions. The experimental results show the rate of aperture change with time, and the predictions are the relation between the rate of aperture change and the contact-area ratio with various ratios of r_c and r_f .

either an unaccounted contribution of the dissolution at the fracture void walls or from an underestimation of the assumed fracture contact area, which should be further examined.

4. Conclusions

In this work, the long-term evolution of the permeability in intact/fractured sandstone and fractured mudstone samples has been measured so as to examine the effects of the prescribed confining pressure, temperature, and permeant exerted on the changes in permeability. The permeability was measured intermittently for more than 1000 days, and the results were reinforced by measurements of the effluent element concentrations (i.e., ICP-AES and IC) and petrographic and microstructural observations (SEM-EDX, XRD, XRF, and microfocus X-ray CT).

In the intact sandstone samples, the permeability increased with time. The sample dimensions changed little or even contracted after the experiments. The increase in permeability resulted from the increase in pore volume induced by the free-face dissolution. The observations by microfocus X-ray CT indicated that the frequency of the pores with a radius ranging from 10 to 60 μm decreased, and that of the pores with a diameter of more than 60 μm increased, which may support the observed increase in permeability. Moreover, the preferential dissolution of the dolomite cements may have contributed to the increase in pore volume. The evaluation of the dimensionless Damkohler number revealed that the dissolved materials are flushed out of the rock samples during each permeability experiment. Subsequently, the pore volume gradually increased with time and it may have taken several hundred days to observe a measurable increase in

permeability. The mismatch of the changes in permeability between the measurements and the predictions, evaluated by the Kozeny–Carman equation by considering the measured concentrations, implies that the gradual increase in permeability may have been induced by the formation of preferential flow paths. Similarly, by taking account of the measured concentrations, the contribution of net dissolution to the changes in permeability in the fractured sandstone and mudstone samples was evaluated in terms of the rate of aperture change, concluding that the observed decrease in permeability was most likely due to the dissolution at the contact areas and the corresponding compaction of the fractures.

Once again, the permeability was measured for more than 1000 days for almost all the rock samples, but the changes, either increases or decreases, were roughly 1 order of magnitude at the most, as compared to the initial values. Deionized water, when used as a permeant, should be much more capable of dissolving rock-forming minerals than in situ groundwater, if chemically under neutral conditions. In other words, the permeability experiments adopted in this work have been conducted under more severe conditions than exist in natural environments, considering the integrity of natural reservoirs (i.e., rocks) used for the long-term isolation of radioactive waste and anthropogenic CO₂. Nevertheless, the increase in permeability in the intact samples, observed over 1000 days, was only 1 order of magnitude relative to the initial values. In the fractured samples, the permeability generally decreased with time, which is still better from the viewpoint of reservoir integrity. As a future study, long-term permeability experiments using in situ groundwater and high and low pH solutions as the permeant will be conducted to examine the effects on the rock permeability of interest.

Acknowledgments

A part of this research project has been conducted as regulatory supporting research funded by the Nuclear Regulation Authority, Japan. It has also been supported by JSPS KAKENHI grant 23360401 and 24560602, the Ministry of Economy, Trade and Industry (METI), and the Basic Research and Development Project of the Korea Institute of Geoscience and Mineral Resources (KIGAM, Project Code No.GP2015-010), which was funded by the Ministry of Science, ICT & Future Planning, Korea. Their support is gratefully acknowledged. The authors also wish to express their great thanks to Saho Kikuchi for her help with the experimental portion of this study. Moreover, the authors greatly appreciate the efforts of the Editors and the three reviewers for their thorough reviews and constructive comments, which helped the authors to improve the manuscript. The data used in this work are available upon request from the authors.

References

- Atkinson, B. K. (1984), Subcritical crack growth in geological materials, *J. Geophys. Res.*, *89*, 4077–4114.
- Atkinson, B. K., and P. G. Meredith (1987), The theory of subcritical crack growth with applications to minerals and rocks, in *Fracture Mechanics of Rock*, edited by B. K. Atkinson, pp. 111–166, Academic, London, U. K.
- Bear, J. (1972), *Dynamics of Fluids in Porous Media*, 166 pp., Dover, N. Y.
- Bjorkum, P. A. (1996), How important is pressure in causing dissolution of quartz in sandstones?, *J. Sediment. Res.*, *66*(1), 147–154.
- Brantut, N., M. J. Heap, P. G. Meredith, and P. Baud (2013), Time-dependent cracking and brittle creep in crustal rocks: A review, *J. Struct. Geol.*, *52*, 17–43.
- Croizé, D., F. Renard, K. Bjørlykke, and D. K. Dysthe (2010), Experimental calcite dissolution under stress: Evolution of grain contact microstructure during pressure solution creep, *J. Geophys. Res.*, *115*, B09207, doi:10.1029/2010JB000869.
- Croizé, D., F. Renard, and J.-P. Gratier (2013), Compaction and porosity reduction in carbonates: A review of observations, theory, and experiments, in *Advances in Geophysics*, chap. 3, vol. 54, edited by R. Dmowska, pp. 181–238, Elsevier, Mass.
- Dawson, G. K. W., J. K. Pearce, D. Biddle, and S. D. Golding (2015), Experimental mineral dissolution in Berea Sandstone reacted with CO₂ or SO₂–CO₂ in NaCl brine under CO₂ sequestration conditions, *Chem. Geol.*, *399*, 87–97.
- Demange, M. A. (2012), *Mineralogy for Petrologists: Optics, Chemistry and Occurrences of Rock-Forming Minerals*, 218 pp., CRC Press, Fla.
- Dewers, T., and A. Hajash (1995), Rate laws for water-assisted compaction and stress-induced water-rock interaction in sandstones, *J. Geophys. Res.*, *100*, 13,093–13,112.
- Dove, P. M., and D. A. Crerar (1990), Kinetics of quartz dissolution in electrolyte solutions using a hydrothermal mixed flow reactor, *Geochim. Cosmochim. Acta*, *54*, 955–969.
- Durham, W. B., W. L. Bourcier, and E. A. Burton (2001), Direct observation of reactive flow in a single fracture, *Water Resour. Res.*, *37*, 1–12.
- Elkhoury, J. E., P. Ameli, and R. L. Detwiler (2013), Dissolution and deformation in fractured carbonates caused by flow of CO₂-rich brine under reservoir conditions, *Int. J. Greenhouse Gas Control*, *16S*, S203–S215.
- Fourrier, R. O., and J. J. Rowe (1977), The solubility of amorphous silica in water at high temperatures and high pressures, *Am. Mineral.*, *62*, 1052–1056.
- Freddi, C. N., and H. S. Fogler (1999), Optimum conditions for wormhole formation in carbonate porous media: Influence of transport and reaction, *SPE J.*, *4*, 196–205.
- Gangi, A. F. (1978), Variation of whole and fractured porous rock permeability with confining pressure, *Int. J. Rock Mech. Min. Sci. Geomech. Abstr.*, *15*, 249–257.
- Graton, L. C., and H. J. Fraser (1935), Systematic packing of spheres, *J. Geol.*, *43*, 785–909.
- Hama, K., T. Kunimaru, R. Metcalfe, and A. J. Martin (2007), The hydrogeochemistry of argillaceous rock formations at the Horonobe URL site, Japan, *Phys. Chem. Earth*, *32*, 170–180.
- Hung, K. M., A. D. Hill, and K. Sepehrmoori (1989), A mechanistic model of wormhole growth in carbonate matrix acidizing and acid fracturing, *J. Pet. Technol.*, *40*, 59–66.
- Ishibashi, T., T. P. McGuire, N. Watanabe, N. Tsuchiya, and D. Elsworth (2013), Permeability evolution in carbonate fractures: Competing roles of confining stress and fluid pH, *Water Resour. Res.*, *49*, 2828–2842, doi:10.1002/wrcr.20253.
- Kalia, N., and V. Balakotaiah (2009), Effect of medium heterogeneities on reactive dissolution of carbonates, *Chem. Eng. Sci.*, *64*, 376–390.
- Kurikami, H., R. Takeuchi, and S. Yabuuchi (2008), Scale effect and heterogeneity of hydraulic conductivity of sedimentary rocks at Horonobe URL site, *Phys. Chem. Earth*, *33*, S37–S44.
- Lawn, B. R., and T. R. Wilshaw (1975), *Fracture of Brittle Solids*, Cambridge Univ. Press, Cambridge, U. K.
- Lindquist, W. B., and A. Venkatarangan (1999), Investigating 3D geometry of porous media from high resolution images, *Phys. Chem. Earth Part A*, *25*, 593–599.
- Lindquist, W. B., S.-M. Lee, D. A. Coker, K. W. Jones, and P. Spanne (1996), Medial axis analysis of void structure in three-dimensional tomographic images of porous media, *J. Geophys. Res.*, *101*, 8297–8310.
- Lockner, D. A. (1993), Room temperature creep in saturated granite, *J. Geophys. Res.*, *98*, 475–487.

- Lockner, D. A. (1995), Rock failure, in *Rock Physics & Phase Relations: A Handbook of Physical Constants*, edited by T. J. Ahrens, pp. 127–147, American Geophysical Union, Washington, D. C.
- Masuda, K. (2001), Effects of water on rock strength in a brittle regime, *J. Struct. Geol.*, *23*, 1653–1657.
- Moore, D. E., D. A. Lockner, and J. D. Byerlee (1994), Reduction of permeability in granite at elevated-temperatures, *Science*, *265*(5178), 1558–1561.
- Mozley, P. S. (1989), Relation between depositional environment and the elemental composition of early diagenetic siderite, *Geology*, *17*, 704–706.
- Neveux, L., D. Grgic, C. Carpentier, J. Pironon, L. Truche, and J. P. Girard (2014a), Experimental simulation of chemomechanical processes during deep burial diagenesis of carbonate rocks, *J. Geophys. Res. Solid Earth*, *119*, 984–1007, doi:10.1002/2013JB010516.
- Neveux, L., D. Grgic, C. Carpentier, J. Pironon, and J. P. Girard (2014b), Influence of hydrocarbon injection on the compaction by pressure solution of a carbonate rock: An experimental study under triaxial stresses, *Mar. Pet. Geol.*, *55*, 282–294.
- Panga, M., M. Ziauddin, and V. Balakotaiah (2005), Two-scale continuum model for simulation of wormholes in carbonate acidization, *AIChE J.*, *51*, 3231–3248.
- Piggott, A. R., and D. Elsworth (1993), Laboratory assessment of the equivalent apertures of a rock fracture, *Geophys. Res. Lett.*, *30*, 1387–1390.
- Polak, A., D. Elsworth, H. Yasuhara, A. Grader, and P. Halleck (2003), Permeability reduction of a natural fracture under net dissolution by hydrothermal fluids, *Geophys. Res. Lett.*, *30*(20), 2020, doi:10.1029/2003GL017575.
- Polak, A., D. Elsworth, J. Liu, and A. S. Grader (2004), Spontaneous switching of permeability changes in a limestone fracture with net dissolution, *Water Resour. Res.*, *40*, W03502, doi:10.1029/2003WR002717.
- Raj, R. (1982), Creep in polycrystalline aggregates by matter transport through a liquid phase, *J. Geophys. Res.*, *87*, 4731–4739.
- Revil, A. (1999), Pervasive pressure-solution transfer: A poro-visco-plastic model, *Geophys. Res. Lett.*, *26*, 255–258.
- Robin, P.-Y. F. (1978), Pressure solution at grain to grain contacts, *Geochim. Cosmochim. Acta*, *42*, 1383–1389.
- Røyne, A., J. Bisschop, and D. K. Dysthe (2011), Experimental investigation of surface energy and subcritical crack growth in calcite, *J. Geophys. Res.*, *116*, B04204, doi:10.1029/2010JB008033.
- Rutter, E. H. (1976), The kinetics of rock deformation by pressure solution, *Philos. Trans. R. Soc. London A*, *283*, 203–219.
- Rutter, E. H. (1983), Pressure solution in nature, theory and experiment, *J. Geol. Soc. London*, *140*(5), 725–740.
- Salehikhoo, F., L. Li, and S. L. Brantley (2013), Magnesite dissolution rates at different spatial scales: The role of mineral spatial distribution and flow velocity, *Geochim. Cosmochim. Acta*, *108*, 91–106.
- Scholz, C. H. (1990), *The Mechanics of Earthquakes and Faulting*, Cambridge Univ. Press, Cambridge, U. K.
- Spiers, C. J., S. De Meer, A. R. Niemeijer, and X. Zhang (2003), *Kinetics of Rock Deformation by Pressure Solution and the Role of Thin Aqueous Films*, *Front. Sci. Ser.*, pp. 129–158, Universal Acad. Press, Tokyo.
- Szymczak, P., and A. J. C. Ladd (2009), Wormhole formation in dissolving fractures, *J. Geophys. Res.*, *114*, B06203, doi:10.1029/2008JB006122.
- Tachi, Y., K. Yotsuji, Y. Sida, and M. Yui (2011), Diffusion and sorption of Cs^+ , I^- and HTO in samples of the argillaceous Wakkanai Formation from the Horonobe URL, Japan: Clay-based modeling approach, *Geochim. Cosmochim. Acta*, *75*, 6742–6759.
- Tester, J. W., W. G. Worley, B. A. Robinson, C. O. Grigsby, and J. L. Feerer (1994), Correlating quartz dissolution kinetics in pure water from 25 to 625°C, *Geochim. Cosmochim. Acta*, *58*, 2407–2420.
- Walsh, S. D. C., H. E. Mason, W. L. Du Frane, and S. A. Carroll (2014), Experimental calibration of a numerical model describing the alteration of cement/caprock interfaces by carbonated brine, *Int. J. Greenhouse Gas Control*, *22*, 176–188.
- Weyl, P. K. (1959), Pressure solution and force of crystallization—A phenomenological theory, *J. Geophys. Res.*, *64*, 2001–2025.
- Witherspoon, P. A., J. S. Y. Wang, K. Iwai, and J. E. Gale (1980), Validity of cubic law for fluid flow in a deformable rock fracture, *Water Resour. Res.*, *16*, 1016–1024.
- Yasuhara, H., and D. Elsworth (2008), Compaction of a rock fracture moderated by competing roles of stress corrosion and pressure solution, *Pure Appl. Geophys.*, *165*, 1289–1306.
- Yasuhara, H., D. Elsworth, and A. Polak (2004), Evolution of permeability in a natural fracture: Significant role of pressure solution, *J. Geophys. Res.*, *109*, B03204, doi:10.1029/2003JB002663.
- Yasuhara, H., A. Polak, Y. Mitani, A. Grader, P. Halleck, and D. Elsworth (2006), Evolution of fracture permeability through fluid-rock reaction under hydrothermal conditions, *Earth Planet. Sci. Lett.*, *244*, 186–200.
- Yasuhara, H., K. Ohfuji, H. Kinoshita, D. S. Lee, S. Nakashima, and K. Kishida (2011), Temporal alteration of fracture permeability in granite under hydrothermal conditions and its interpretation by coupled chemo-mechanical model, *Appl. Geochem.*, *26*, 2074–2088.
- Zhang, X., C. J. Spiers, and C. J. Peach (2010), Compaction creep of wet granular calcite by pressure solution at 28°C to 150°C, *J. Geophys. Res.*, *115*, B09217, doi:10.1029/2008JB005853.
- Zhang, X., C. J. Spiers, and C. J. Peach (2011), Effects of pore fluid flow and chemistry on compaction creep of calcite by pressure solution at 150°C, *Geofluids*, *11*(1), 108–122.
- Zubtsov, S., F. Renard, J. P. Gratier, R. Guiguet, D. K. Dysthe, and V. Traskine (2004), Experimental pressure solution compaction of synthetic halite/calcite aggregates, *Tectonophysics*, *385*, 45–57.